



Mikołaj Jaszczur, BSc

Comparison of planar and spherical tunnel faces

Master's Thesis

Submitted in fulfilment of the requirements for the degree of

Diplom-Ingenieur

Master's programme Civil Engineering, Geotechnics and Hydraulics

at

Graz University of Technology

O. Univ.-Prof. Dipl.-Ing. Dr. mont. Wulf Schubert

Institute of Rock Mechanics and Tunnelling

Graz University of Technology

Dipl.-Ing. Michael Rudolf Henzinger

Institute of Rock Mechanics and Tunnelling

Graz University of Technology

Graz, November 2017

EIDESSTATTLICHE ERKLÄRUNG

AFFIDAVIT

Ich erkläre an Eides statt, dass ich die vorliegende Arbeit selbstständig verfasst, andere als die angegebenen Quellen/Hilfsmittel nicht benutzt, und die den benutzten Quellen wörtlich und inhaltlich entnommenen Stellen als solche kenntlich gemacht habe. Das in TUGRAZonline hochgeladene Textdokument ist mit der vorliegenden Masterarbeit identisch.

I declare that I have authored this thesis independently, that I have not used other than the declared sources/resources, and that I have explicitly marked all material which has been quoted either literally or by content from the used sources. The text document uploaded to TUGRAZonline is identical to the present master's thesis.

Datum / Date

Unterschrift / Signature

Acknowledgements

My first thank goes to my supervisor Professor Dr. Wulf Schubert, head of the Institute of Rock Mechanics and Tunnelling at the Graz University of Technology. I would like to thank him for the opportunity to prepare this master's thesis.

Special thanks to Dipl.-Ing. Michael Henzinger for his help and assistance during the preparation of this work.

Finally, I would like to thank my father Robert for his support and encouragement during my studies in Poland, Germany, Austria and Taiwan.

Abstract

Tunnels driven in poor ground conditions require additional measures to maintain the stability of the heading. While the face instability in a poor ground always pose an issue, changing the face from a planar to a spherical shape may contribute to a safer and faster construction. Up to now there have been only few attempts to investigate the behaviour of spherical tunnel faces. Thus, a firm statement concerning the performance of the spherical face cannot be made. This thesis compares the behaviour of planar and spherical faces in conventional tunnelling. For the purpose of this work a three-dimensional numerical model using a FDM software was prepared. With the application of elastic perfect-plastic constitutive models a realistic behaviour of the ground was achieved. The calculations spanned the range of sequential and full face excavations with and without a tunnel support. The effectiveness of the spherical face was described in terms of a dimensionless parameter. This study showed that the spherical face experiences lower longitudinal deformations than the planar one. The volume of the failure zone ahead of the heading is significantly reduced. On top of that, the application of a tunnel support enhances the effectiveness of the spherical face. As such, comparing with the planar face, longitudinal face displacements can be reduced by a factor of five. Indeed, the findings of this work suggest that in specific ground conditions the application of the spherical face may eliminate the necessity of a face bolting. As a result, material demands can be reduced and excavation speed notably increased.

Keywords: Spherical face, Planar face, Tunnel support, Comparison, FDM, Arching, Stress, Displacement, Plastic radius, NATM

Kurzfassung

Tunnelvortrieb in schlechten Bodenverhältnissen erfordert zusätzliche Maßnahmen, um die Stabilität der Ortsbrust sicherzustellen und die Verformungen in einem tolerierbaren Bereich zu halten. Bis heute gab es nur wenige Untersuchungen zum Verhalten einer sphärischen Ortsbrust. Somit kann keine eindeutige Aussage über das Verhalten einer sphärischen Brust gemacht werden. Diese Masterarbeit beinhaltet die Gegenüberstellung der Verhalten von vertikaler und sphärischer Ortsbrust im konventionellen Tunnelbau. Im Rahmen dieser Arbeit wurde ein dreidimensionales numerisches Modell unter Verwendung einer FDM-Software erarbeitet. Mit der Anwendung elastischer perfekt-plastischer Stoffgesetze wurde ein realistisches Verhalten des Bodens erreicht. Die Berechnungen umfassten den Voll- sowie Teilausbruch mit und ohne Tunnelstützung. Die Wirksamkeit einer sphärischen Ortsbrust wurde mit Hilfe eines dimensionslosen Faktors beschrieben. Diese Studie zeigte, dass die sphärische Ortsbrust geringere Deformationen erfährt als eine vertikale Ortsbrust. Das Volumen der plastischen Zonen vor der Ortsbrust wird deutlich reduziert. Durch den Einbau einer Tunnelschale können die Verschiebungen im Vergleich zu einer ebenen Tunnelortsbrust um einen Faktor von fünf reduziert werden. Diese Arbeit zeigt auf, dass durch die Anwendung einer sphärischen Ortsbrust die Notwendigkeit der Ortsbrustankerung in bestimmten Bodenverhältnissen eliminiert werden kann. Als Folge davon können die Materialanforderungen reduziert und die Vortriebsleistung deutlich erhöht werden.

Schlüsselwort: Sphärische Ortsbrust, Vertikale Ortsbrust, Tunnelstützung, Gegenüberstellung, FDM, Gewölbewirkung, Spannung, Tunnelverformung, Plastische Zone, NÖT

Table of contents

1	Introduction	1
1.1	State of the art.....	1
1.2	Aim of the work	6
1.3	Outline	6
2	Methodology	8
2.1	Numerical model	8
2.2	Material characteristic	10
2.3	Modelling sequence	13
2.4	Data analysis	18
2.5	Model validation	19
3	Results	23
3.1	Failure mechanism.....	23
3.2	Unsupported tunnel.....	25
3.3	Shotcrete lining	31
3.4	Shotcrete lining with face bolting.....	39
4	Discussion	42
5	Conclusion	48
5.1	Summary.....	48
5.2	Outlook	49
	Bibliography	51
	Appendix	54

List of figures

Figure 1.1: a) Three-dimensional failure mechanism (Horn, 1961); b) Forces acting on the prism and the sliding wedge (Horn, 1961).....	2
Figure 1.2: Two- and three-dimensional failure mechanisms proposed by Krause (1987): a) Circular; b) Semi-circular; c) Spherical.....	2
Figure 1.3: Collapse mechanisms proposed by Leca & Dormieux (1990): a) Two-block mechanism; b) Single-block mechanism.....	3
Figure 1.4: Tunnel face geometry according to Kolymbas (1998)	4
Figure 2.1: The dimensions of the numerical model and the global coordinate system	9
Figure 2.2: Model boundary conditions and the extent of influenced zone	10
Figure 2.3: Description of the parameter r_s	14
Figure 2.4: Unsupported full face excavation with a varying parameter r_s	16
Figure 2.5: Unsupported sequential excavation: a) With supporting core and vertical face; b) Without core but with varying parameter r_s	16
Figure 2.6: Supported full face excavation: a) Planar face; b) Spherical face.....	17
Figure 2.7: Supported sequential excavation: a) With supporting core; b) Without supporting core.....	17
Figure 2.8: Comparison of the secondary stress state yielded with <i>FLAC3D</i> and according to Feder & Arwanitakis (1976).....	20
Figure 2.9: Comparison of the secondary stress state ahead of the face yielded with <i>FLAC3D</i> and according to Kolymbas (1998).....	21
Figure 2.10: Comparison of internal forces in the lining yielded with <i>FLAC3D</i> and according to the analytical solutions of Einstein & Schwartz (1979) and Ahrens et al. (1982): a) Normal forces; b) Bending moments	22
Figure 3.1: a) Failure mechanism with a planar face; b) Vertical stresses as a function of depth for different positions ahead of the face	24
Figure 3.2: a) Failure mechanism with a spherical face; b) Vertical stresses as a function of depth for different positions ahead of the face.....	24
Figure 3.3: Secondary stress state at the face as a function of face distance. Unsupported full face excavation: a) Model 1; b) Model 2; c) Model 3; d) Model 4; e) Legend	26

Figure 3.4: State of deformation at the face. Unsupported full face excavation: a) Model 1; b) Model 2; c) Model 3; d) Model 4.....	27
Figure 3.5: Plastic state at the face. Unsupported full face excavation: a) Model 1; b) Model 2; c) Model 3; d) Model 4	28
Figure 3.6: Plastic radius as a function of face distance. Unsupported full face excavation	28
Figure 3.7: Secondary stress state at the face as a function of face distance. Unsupported sequential excavation: a) Model A; b) Model B; c) Model C; d) Model D	29
Figure 3.8: Comparison of face displacement. Unsupported sequential excavation: a) Model A; b) Model B; c) Model C; d) Model D	30
Figure 3.9: Plastic state at the face. Unsupported sequential excavation: a) Model A; b) Model B; c) Model C; d) Model D	31
Figure 3.10: Secondary stress state at the face as a function of face distance. Supported full face excavation: a) Model 1; b) Model 2; c) Model 3; d) Model 4	32
Figure 3.11: Vertical stresses as a function of the depth shown for different positions ahead of the face. Supported full face excavation: a) Vertical face; b) Spherical face.....	33
Figure 3.12: Internal forces in the face support. Supported full face excavation: a) Model 1; b) Model 2; c) Model 3; d) Model 4.....	34
Figure 3.13: Internal forces in the support at the tunnel wall. Supported full face excavation: a) Model 1; b) Model 2; c) Model 3; d) Model 4	35
Figure 3.14: State of deformation at the face. Supported full face excavation: a) Model 1; b) Model 2; c) Model 3; d) Model 4.....	35
Figure 3.15: Plastic zone around the excavation. Supported full face excavation: a) Model 1; b) Model 2; c) Model 3; d) Model 4	36
Figure 3.16: Comparison of the plastic radius. Supported full face excavation	37
Figure 3.17: Secondary stress states as a function of face distance. Supported sequential excavation: a) Model A; b) Model B; c) Model C; d) Model D	37
Figure 3.18: State of deformation at the face. Supported sequential excavation: a) Model A; b) Model B; c) Model C; d) Model D.....	38
Figure 3.19: Plastic state at the tunnel face. Supported sequential excavation: a) Model A; b) Model B; c) Model C; d) Model D	39

Figure 3.20: State of deformation at the face. Full face excavations supported with shotcrete and bolts: a) Model 1; b) Model 2; c) Model 3; d) Model 4	40
Figure 3.21: Plastic state at the face with shotcrete and face bolts. Full face excavations: a) Model 1; b) Model 2; c) Model 3; d) Model 4	41
Figure 3.22: Comparison of plastic radius at the face supported with shotcrete and bolts. Full face excavations	41
Figure 4.1: The reduction factor d_{red} as a function of the r_s . Full face excavations	44
Figure 4.2: The reduction factor d_{red} depending on the type of the sequential excavation	44
Figure 4.3: a) Full face excavation supported with shotcrete (model A); b) Full face excavation supported with shotcrete and face bolts (model B); c) Spherical full face excavation supported with shotcrete (model C); d) Top heading excavation supported with shotcrete and supporting core (model D)	45
Figure 4.4: Deformation at the face with the Mohr-Coulomb. Model A	46
Figure 4.5: Deformation at the face with the Mohr-Coulomb: a) Model B; b) Model C	46
Figure 4.6: Deformation at the face with the Mohr-Coulomb. Model D	47
Figure 4.7: Deformation at the face with the Plastic Hardening. Model A	47
Figure 4.8: Deformation at the face with the Plastic Hardening: a) Model B; b) Model C	47

List of tables

Table 2.1: The dimensions of the numerical model	9
Table 2.2: Sets of ground parameters valid with Mohr-Coulomb model	10
Table 2.3: Set of ground parameters valid with Plastic Hardening model	11
Table 2.4: Input parameters of the shotcrete lining	12
Table 2.5: Input parameters of the face bolts	12
Table 2.6: The dimensions of the excavation parts valid for a sequential excavation (e.g. models A, B, C and D)	17
Table 2.7: Control points	18
Table 2.8: Stress state at the level of tunnel crown and invert	20

Abbreviations

FDM.....	Finite Difference Method
FE.....	Finite Element
MC.....	Mohr-Coulomb
NATM	New Austrian Tunnelling Method
PH	Plastic-Hardening
SpC	Sprayed Concrete
2D.....	two-dimensional
3D.....	three-dimensional

Symbols

Capital letters

A	cross sectional area of grouted bolts [m ²]
D	tunnel diameter [m]
E	elastic modulus of the ground [MPa]
E _{50,ref}	secant modulus for primary triaxial loading [MPa]
E _{an}	elastic modulus bolts [MPa]
E _{oed,ref}	tangent modulus for oedometric loading [MPa]
E _{spc}	Young's modulus shotcrete [MPa]
E _{ur,ref}	secant modulus for un- and reloading [MPa]
G ₁	Dead weight of vertical prism [-]
G ₂	Dead weight of inclined wedge [-]
H ₁	Model height (overburden) [m]
H ₂	Model depth [m]
K ₀	coefficient of earth pressure at rest [-]
L	model length [m]
L _a	length of bolts [m]
M	bending moment in tunnel lining [kNm]
N	normal force in tunnel lining [kN]
P	vertical load on the sliding wedge [-]
R	tunnel radius [m]
R ₁	Stabilizing force due to friction along the vertical prism [-]
R ₂	Stabilizing force acting on the sliding surface [-]
R _f	failure ratio [-]
S	face support [-]
T ₂	frictional resistance force along the sliding surface [-]
W	model width [m]

Lower case letters

cground cohesion [kPa]
c_ggrout cohesive strength [kPa]
d_{red}ratio of longitudinal displacement of spherical and vertical faces [-]
k_ggrout stiffness [MPa]
k_pearth pressure coefficient [-]
mexponent of the Ohde/Janbu law [-]
p_ggrout perimeter [m]
p_isupport pressure [kPa]
p_{ref}reference pressure [MPa]
r_odistance from the face [m]
r_pplastic radius [m]
r_ssphere radius [m]
t_fthickness of shotcrete at the face [m]
t_wthickness of shotcrete in the wall [m]
xdimension along the x-axis [m]
ydimension along the y-axis [m]
zdimension along the z-axis [m]

Greek letters

γunit weight [kN/m ³]
νPoisson's ratio of ground mass [-]
ν_{sh}Poisson's ratio of shotcrete [-]
ν_{ur}Poisson's ratio unloading-reloading [-]
σ_0initial stress [MPa]
σ_rradial stress [MPa]
$\sigma_{rad,el}$elastic part of radial stress [MPa]
$\sigma_{rad,pl}$plastic part of radial stress [MPa]
σ_ttangential stress [MPa]
$\sigma_{tan,el}$elastic part of tangential stress [MPa]
$\sigma_{tan,pl}$plastic part of tangential stress [MPa]
σ_yhorizontal stress [MPa]
σ_zvertical stress [MPa]
φfriction angle [°]
ψdilatancy angle [°]
ωinclination of the sliding wedge [°]

1 Introduction

1.1 State of the art

1.1.1 Theoretical methods concerning tunnel face stability

The tunnel face is considered to play an essential role in the stability of the whole tunnel. To date several attempts have been made to describe the behaviour of the advancing tunnel face. Theoretical models, numerical investigations and small-scale laboratory tests have been carried out as part of this research.

The first method was developed by Horn (1961). It was a three-dimensional model based on the Terzaghi's silo theory. As presented in Figure 1.1a, Horn's failure mechanism consists of a vertical shaft and an inclined wedge. The dimensions of the blocks depend on the tunnel size and overburden. The pressure acting on the wedge is assumed using the Rankine's lateral earth pressure theory. Figure 1.1b shows the forces acting on the sliding wedge and the prism. The dead weight of the overlaying prism causes the wedge to slide, whereas forces governed by friction and cohesion stabilize the blocks. Safety against sliding is ensured when the resisting forces along the prism and wedge exceed the driving forces. Note that Horn's model poses numerous limitations. Firstly, it is only valid for a homogenous, isotropic ground. Secondly, the calculation bases on a limit equilibrium method. Finally, only one failure mechanism has been assumed.

In an attempt to validate Horn's findings several models have been developed. For example, Atkinson & Potts (1977) demonstrated an alternative method to obtain the face support pressure for tunnels driven in cohesionless soils. Atkinson & Mair (1981) discussed drained and undrained calculations for tunnelling in soft ground. Krause (1987) introduced two- and three-dimensional, oval shaped failure mechanisms (see Figure 1.2). In his analysis, the author calculated the minimum support pressure by performing a series of limit-equilibrium analyses. In another major study, Leca & Dormieux (1990) developed an upper and lower bound solution based on the limit equilibrium analysis. Their collapse mechanism consists of either one (see Figure 1.3b) or two rigid, conically shaped blocks (see Figure 1.3a). Dimensions of the elements depend on the ground strength parameters. Sternath & Baumann (1997) suggested that the collapse geometry of NATM-driven tunnels could be described as a cylinder-shaped prism. They noted that the unsupported length d_c governs the dimensions of a failure mechanism. The authors, like Broere (2001), identified the drawbacks of Horn's model and extended its application to a layered ground.

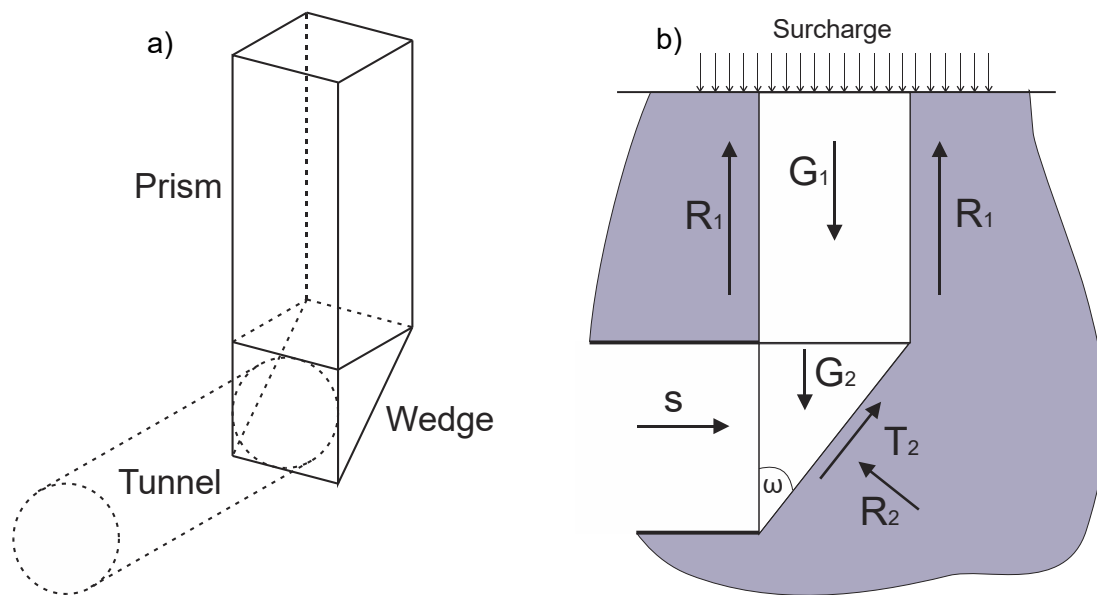


Figure 1.1: a) Three-dimensional failure mechanism (Horn, 1961); b) Forces acting on the prism and the sliding wedge (Horn, 1961)

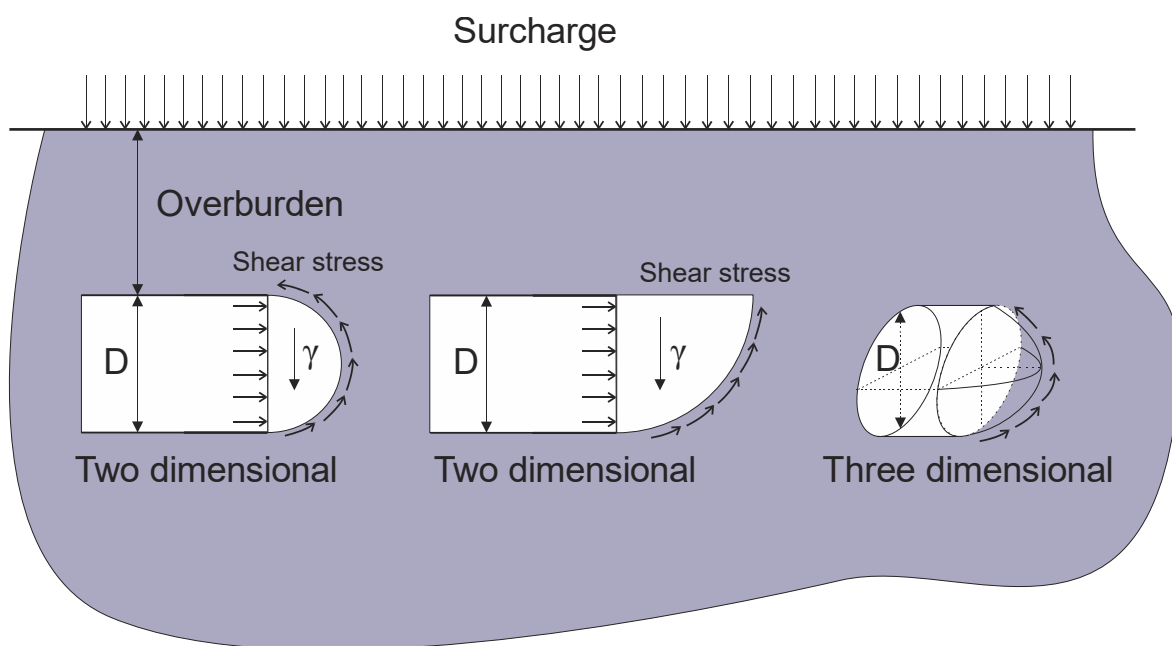


Figure 1.2: Two- and three-dimensional failure mechanisms proposed by Krause (1987): a) Circular; b) Semi-circular; c) Spherical

In recent studies, Vermeer et al. (2002) established a function relating the face support pressure to the ground strength parameters and tunnel dimensions. In another major work, Schubert & Schweiger (2004) looked into the stress rearrangement at the tunnel heading. By presenting two collapse mechanisms, the authors confirmed the geometries proposed previously by Krause. Finally, Ruse (2004) performed numerous three-dimensional calculations using a finite element software. The author derived an

empirical formula to evaluate the minimum support pressure for different ground and tunnel characteristics. His study showed that for a ground with $\varphi > 20^\circ$ the impact of overburden, surface load or dilatancy angle on the failure pressure could be neglected. In fact, the author established a simplified relationship to obtain the safety factor concerning the tunnel face stability.

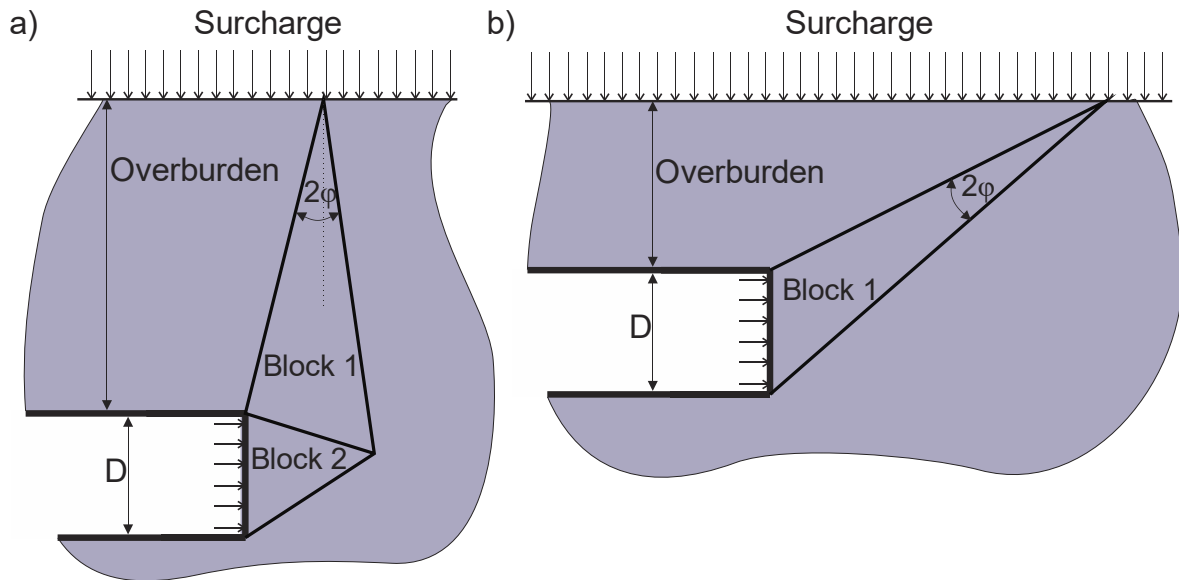


Figure 1.3: Collapse mechanisms proposed by Leca & Dormieux (1990): a) Two-block mechanism; b) Single-block mechanism

1.1.2 Spherical face

Another approach to enhance the face stability is to alter the shape of the heading. For example, Kolymbas (1998) established an analytical solution to obtain the secondary stress state at the face. In his study, the author approximated tunnel face by a sphere (see Figure 1.4). Based on a series of differential equations and assuming a hydrostatic stress state Kolymbas obtained the secondary stresses at the face. The formulas after Kolymbas (1998) describe the elastic stresses:

$$\sigma_{rad,el} = \sigma_0 - (\sigma_0 - p_i) * \left(\frac{r_0}{R}\right)^3 \quad (1.1)$$

$$\sigma_{tan,el} = \sigma_0 + \frac{1}{2}(\sigma_0 - p_i) * \left(\frac{r_0}{R}\right)^3 \quad (1.2)$$

It is apparent that the elastic part of stresses is influenced mainly by the primary stress state. If a tunnel support is applied, stresses will increase by an equivalent support pressure. However, if the ground strength is exceeded, plastic deformations will occur. The

relationships after Kolymbas (1998) to obtain the stress state in the plastic zone are presented in Eq. (1.3) and Eq. (1.4).

$$\sigma_{rad,pl} = (p_i + c * \cot \varphi) \left(\frac{R}{r_0} \right)^{2(k-1)} - c * \cot \varphi \quad (1.3)$$

$$\sigma_{tan,pl} = k_p * \sigma_{rad,pl} + 2c * \frac{\cos \varphi}{1 - \sin \varphi} \quad (1.4)$$

Stresses in the plastic zone are influenced by the ground strength parameters. Kolymbas (1998) attempts to determine the plastic radius at the tunnel heading. The author assumes that at the border between the plastic and elastic zone the stresses must be equal. The formula shown in Eq. (1.5) describes the relation:

$$r_p = r_0 * \left(\frac{\frac{2}{2 * k_p + 1} * \left(\frac{3}{2} * \sigma_0 - 2c * \frac{\cos \varphi}{1 - \sin \varphi} \right) + c * \cot \varphi}{p_i + c * \cot \varphi} \right)^{\frac{1}{2(k_p-1)}} \quad (1.5)$$

Hence, plastic radius is a function of strength parameters c and φ , initial stress state σ_0 , applied support pressure p_i and the earth pressure coefficient k_p . Thus, by knowing the plastic radius, one could obtain the minimum support pressure.

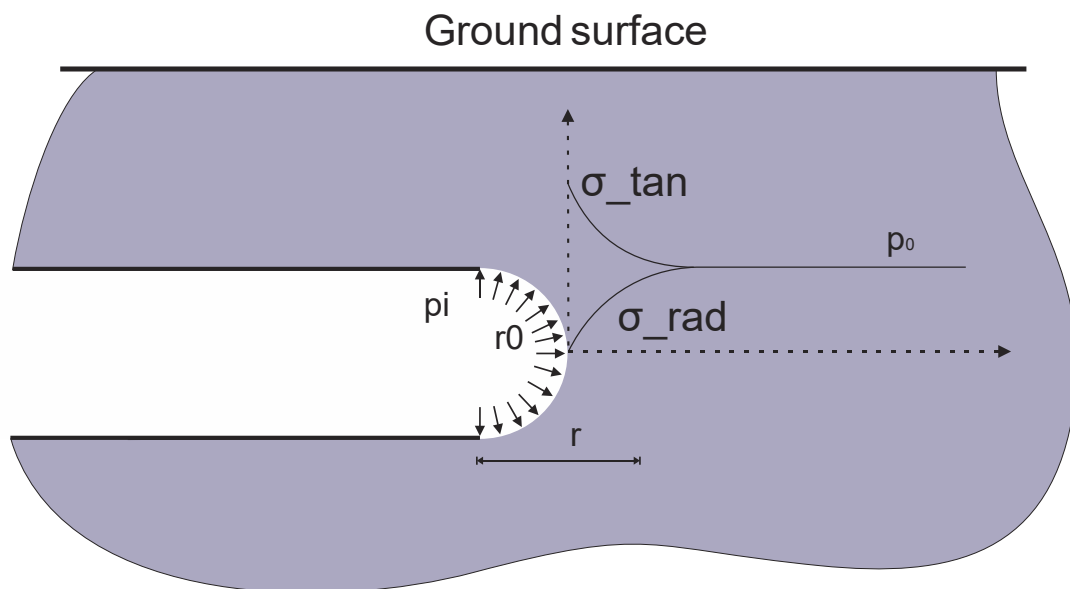


Figure 1.4: Tunnel face geometry according to Kolymbas (1998)

Further studies concerned with the spherical face were based on a numerical analysis and trial excavations. Some researchers, such as Shinji et al. (2004), investigated the behaviour of the spherical face using a FDM software. The author conducted a series

of three-dimensional simulations and compared the behaviour of planar and spherical faces in a poor, squeezing ground. The findings showed that the spherical face experiences lower horizontal deformations than the vertical one. Based on those results the author anticipated a formation of a load-bearing arch near the excavation contour. While this work included plots of deformation, the author did not present the state of secondary stresses. Furthermore, this study failed to consider the extent of the plastic zone around the excavation.

In his analysis of spherical face, Kusumoto et al. (2013) performed a three-dimensional FDM analysis with various excavation patterns. The simulations covered different round lengths as well as numerous types and shapes of excavations. In general, spherical face experienced lower deformations at the crown as well as at the face. The author highlighted different distribution of displacements with both faces. Furthermore, the simulations of the spherical face revealed a notable reduction of stresses in the tunnel support. The author compared those findings with the observations from a trial excavation in the Hachinoshiri Tunnel. Indeed, lower deformations at the crown and in the sidewalls with the spherical face have been reported. Again, the presence of a load-bearing arch near the heading was assumed. While this study was conducted with relatively good ground conditions, no attempt was made to repeat the simulations with a soft ground. Besides, the author did not analyse the behaviour of a tunnel lining at the face.

Finally, Amemiya et al. (2014) published numerous experiences with a spherical face collected during the construction of the Shin-Takahama Tunnel in Japan. The assessment of the face stability was made by calculating the frequency and consequences of rock falls. In addition, Amemiya et al. (2014) compared tunnel deformations and forces induced in the lining. However, the displacements were too low to observe a notable trend. Furthermore, only marginal differences in the shotcrete stresses have been reported. Like the previous researchers, the author suggested an advanced development of a load-bearing arch close to the heading. Though, notable advantages of the spherical face have been mentioned. For example, although the stability of a spherical face is comparable to the vertical face with an auxiliary bench, all the advantages of a full face excavation are maintained. This study, however, poses some limitations. While the work focused on the onsite experiences, a verification of the results obtained onsite by a numerical simulation is missing. Furthermore, the correctness of the stability assessment may be disputable.

1.2 Aim of the work

The effect of a spherical face on the tunnel behaviour has not been fully investigated. Firstly, most of the previous studies have been restricted to only one geometry set. Only Kusumoto et al. (2013) performed an analysis to relate the geometry of a spherical face to the magnitude of displacements. Secondly, only Shinji et al. (2004) carried out numerical calculations assuming poor ground conditions. Thirdly, to date studies have not thoroughly dealt with a description of the face displacements. Although many researchers assumed the presence of a load-bearing arch ahead of the heading, none of them conducted a comprehensive stress analysis. Finally, there has been hardly any work concerned with the extent of the plastic zone ahead of the face. Hence, until now, a firm statement on the effectiveness of this method was not feasible. Therefore, the aim of this work was to provide a numerical basis for an execution of the spherical face onsite. To attain this goal, a number of objectives should be fulfilled:

- To investigate the relationship between the shape of the face and displacement development
- To compare the volume of the plastic zone ahead of the heading
- To analyse the collapse mechanisms taking place with planar and spherical faces
- To compare the location of a load-bearing arch ahead of the heading

1.3 Outline

This thesis is divided into five parts. Chapter 1 illustrates the background and the objectives of this work.

Chapter 2 deals with the methodology. At first, the FDM software used for the purpose of this study is introduced. Then, the model geometry together with the material parameters and constitutive equations are described. Subsection 2.4 introduces the scope of the analysis. This is followed by a description of the modelling sequence. Finally, subsection 2.5 deals with the validation of the model. Within this part, the results of the initial tests have been compared with analytical solutions. Thus, plausibility of the numerical results was verified. Finally, an attempt was made to check the impact of the constitutive model on the results.

Chapter 3 deals with the findings of the simulations. This part has been divided into four sections. At first, the author looked into the failure mechanisms occurring with planar and spherical faces. Thus, the reader has a chance to observe the formation of the load-bearing arch ahead of the heading. Next, chapter 3 presents the results concerning an unsupported tunnel. Stresses, deformations and plastic zones calculated with different face geometries have been compared. The results of simulations with a lined tunnel are the topic of subsection 3.3. Thus, the reader gains a deeper insight into the distribution of internal forces in the support. Finally, subsection 3.4 reveals the findings concerned with a tunnel supported with shotcrete and face bolts.

Chapter 4 discusses the results from the previous section. The author examines the data to qualitatively describe the effects of the spherical face. Finally, an attempt has been made to draw some practice-related conclusions. Additional simulations have been performed to check the validity of the stated hypothesis.

In chapter 5 the conclusion of this work is presented. A brief summary concerns the first part of this chapter. This included findings, which emerged during the course of this work. Finally, in subsection 5.2 an outlook into future research projects is shown.

2 Methodology

2.1 Numerical model

The stress state at the tunnel face is a three-dimensional problem. This means that as a tunnel heading advances, a pre-relaxation occurs ahead of the face. Thus, only a three-dimensional analysis can accurately simulate the ground behaviour at the face. Given the above, the FDM programme “Fast Lagrangian Analysis of Continua in Three Dimensions” (*FLAC^{3D}*) from ITASCA was used. *FLAC^{3D}* provides a series of non-linear constitutive models as well as built-in functions to simulate a tunnel support. Unlike other geotechnical programs, *FLAC^{3D}* features a command-based user interface and a built-in coding language called *FISH*.

Due to the axial symmetry only the right half of the cross section was modelled. The mesh was composed of the *FLAC^{3D}* built-in elements. For the purpose of simplicity, a circular tunnel cross section was chosen.

To date countless studies have been published to set a universal geometry of a 3D numerical model. It is worth to mention the work by Deutsche Gesellschaft für Geotechnik (2012). Wittke (1999), Meißner (1991) and Meißner (1996) published typical model geometries. Yet, those publications present quite conservative values. On one hand, Wittke (1999) suggests a model width of minimum 7R. On the other hand, Ruse (2004) calculated the minimum face pressure with a model of only 4R width. The same model dimensions have been used by Kirsch (2015). In fact, Ruse (2004) showed that model widths greater than 2R do not influence the results significantly. With this in mind, the author performed a series of tests to investigate the impact of the model size of the numerical results. Since the behaviour of the face was the primary interest of this work, the model length has been found to be the most important factor. According to Ruse (2004), the displacements in the zones laying within 2D from the model boundaries are influenced by the artificial boundary conditions. Golser (1999) pointed out that the elements within 2.5D from the model boundary show an error associated with the model edges (see Figure 2.2). Both authors term this part of the model as an “influence length”. As such, Wittke (1984) suggests an influence length of 2D. Considering the above statements, the length of the model was set to 6D. Furthermore, as pointed out by the cross section A-A (see Figure 2.2), the results were analysed in a distance of 3D from both model edges. Thus, the error caused by the artificial boundaries could be excluded. The remaining

dimensions have been either assumed directly after Wittke (1999) or optimised to achieve lower computational times. Table 2.1 presents the chosen values.

The dimensions of elements laying further away from the tunnel axis were gradually increased. This was done to achieve higher accuracy near the tunnel boundaries. Indeed, denser mesh was required where high gradients of stresses and displacements were expected. According to Ruse (2004), the tunnel face should be discretized by at least 10 elements in the transversal direction. On top of that, the author suggests a maximum element length of $0.1D$. The chosen mesh fulfilled both requirements.

Table 2.1: The dimensions of the numerical model

Dimension	Symbol	Recommended	Chosen	
		(Wittke, 1999)	[m]	[-]
Tunnel radius	R	Case specific	5	R
Model width	W	$7 - 9 \cdot R$	30	$6 \cdot R$
Model length	L	$> 10 \cdot R$	60	$12 \cdot R$
Overburden	H_1	Case specific	25	$5 \cdot R$
Model depth	H_2	$5 - 7 \cdot R$	25	$5 \cdot R$

Figure 2.1 shows the orientation of the global coordinate system. The z-axis points upwards, towards the ground surface. The y-axis lays along the tunnel axis and will be later referred as the longitudinal direction. The x-axis is perpendicular to both y- and z-axis and represents the transversal direction.

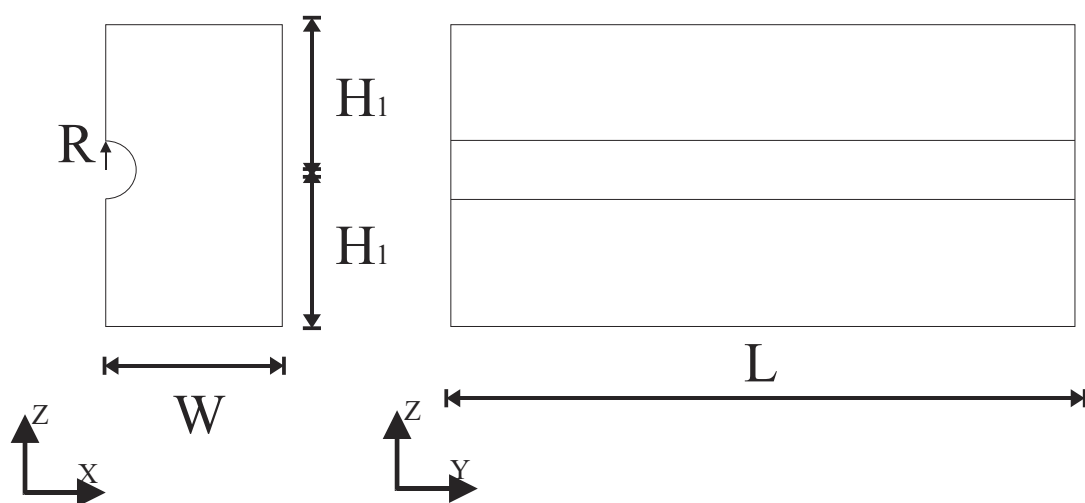


Figure 2.1: The dimensions of the numerical model and the global coordinate system

Fixed model boundaries were applied (see Figure 2.2). Roller supports placed on the model boundaries restricted horizontal movements. The bottom nodes were restrained in the vertical direction. Finally, ground surface was free to displace.

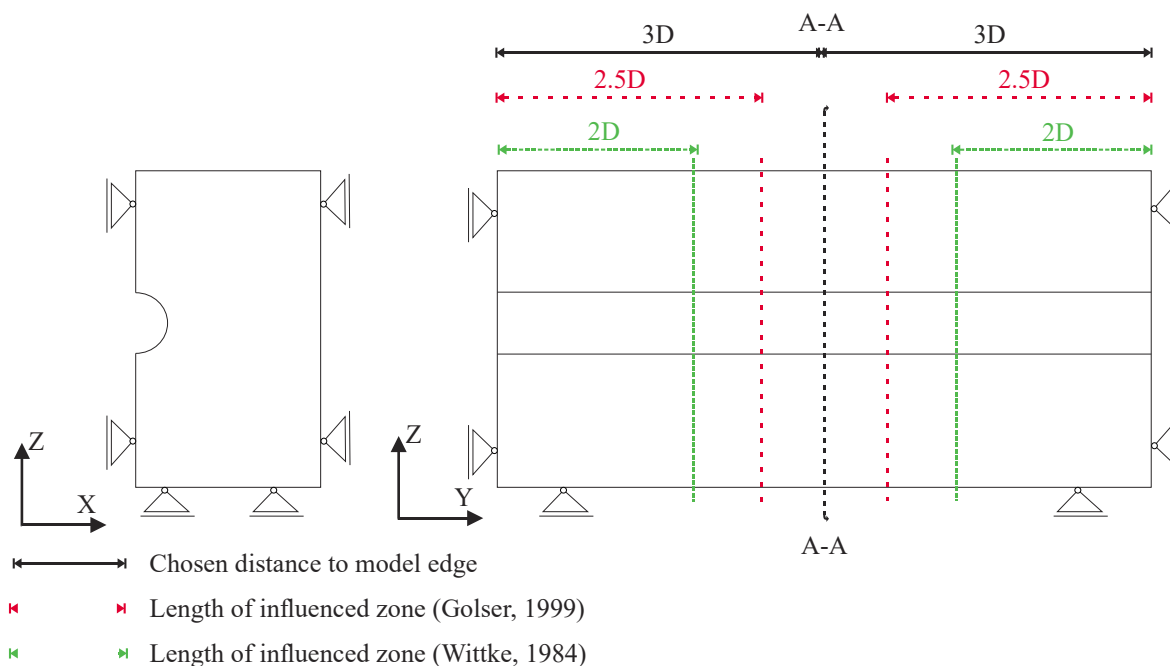


Figure 2.2: Model boundary conditions and the extent of influenced zone

2.2 Material characteristic

2.2.1 Ground mass

For the sake of simplicity, homogenous and isotropic ground conditions were assumed. Stress states have been described in terms of effective stresses. The ground behaviour was simulated by two constitutive equations, namely an elastic-perfectly plastic Mohr-Coulomb and a non-linear Plastic-Hardening. Chapter 3 presents the results obtained with the MC, whereas chapter 4 contains the results with both MC and PH. Table 2.2 and Table 2.3 show the sets of ground parameters for both models. For the purpose of simplicity, the time-dependant ground behaviour such as creep or consolidation was not considered.

Table 2.2: Sets of ground parameters valid with Mohr-Coulomb model

Set no.	φ	c	ν	γ	E	K_0
[-]	[°]	[kPa]	[-]	[kN/m ³]	[MPa]	[-]
1	20	80	0.3	22	120	0.66
2	20	20	0.3	22	100	0.66

Table 2.3: Set of ground parameters valid with Plastic Hardening model

Set no.	φ	c	γ	E_{oed}^{ref}	E_{50}^{ref}	E_{ur}^{ref}	ν_{ur}	p_{ref}	m	R_f	K_0
[-]	[°]	[kPa]	[kN/m ³]	[MPa]	[MPa]	[MPa]	[-]	[MPa]	[-]	[-]	[-]
3	20	20	22	100	100	250	0.2	0.1	0.5	0.9	0.66

The linear-elastic part of the MC model is based on the Hook's law. Elastic strains are governed by the Poisson's ratio and Young's modulus. An assumption of constant, stress-independent stiffness poses an important drawback of the MC. On top of that, the elastic part of the stress-strain relationship is linear. In reality, however, ground exhibits a non-linear behaviour. As a result, the MC model shows limited capabilities. For example, the MC struggles to yield realistic results when the ground is close to a failure state. Besides, calculations with the MC criterion produce a significant heave in the invert. However, simulations with the MC require less computational time due to the simplicity of mathematical description.

A non-linear ground behaviour is taken into account with the application of the Plastic Hardening model. The friction hardening is used to model plastic shear strains, whereas the cap hardening governs the development of plastic volumetric strains. The drawback, of the PH is the necessary input of a detailed ground information (i.e. $E_{oed,ref}$, $E_{ur,ref}$, $E_{50,ref}$, m, ν_{ur} and p_{ref}). Still, the main advantage of the PH model lies in the assumption of a stress dependent stiffness. Thus, a reliable prediction of ground deformations can be achieved. This means that the unrealistic heave in the invert is significantly reduced.

2.2.2 Shotcrete lining

Three-noded shell elements were used to model a tunnel lining. Table 2.4 shows the input parameters. While the tunnel support exhibited a linear-elastic stress-strain behaviour, the material was isotropic. A fixed connection between ground and shotcrete meant that the relative displacements between both elements were restricted. Moreover, a rigid bond between the neighbouring shells allowed a redistribution of stress resultants. This led to a continuous displacement field across the joints. Creep behaviour was neglected because a complex modelling of shotcrete was beyond the scope of this thesis. Finally, for the sake of simplicity, the strength properties of shotcrete were constant during all the simulation steps.

Utilization of shell elements required an additional set of boundary conditions. The displacements of elements lying on the symmetry plane (y-z plane) were restricted in the

normal direction. In addition, the rotation about the axes lying on the global y-z plane was not allowed.

Table 2.4: Input parameters of the shotcrete lining

Property	Symbol	Value	Unit
Young's modulus	E_{SpC}	10500	[MPa]
Poisson's ratio	ν	0.25	[-]
Thickness wall	t_w	0.3	[m]
Thickness face	t_f	0.1	[m]
Unit weight	Γ	24	[kN/m ³]

2.2.3 Face bolting

Built-in cable elements were used to model face bolts. The author chose fully grouted, 12 m long bolts. Table 2.5 presents the set of input parameters. Like shell elements, the bolts exhibited a linear-elastic stress-strain behaviour. The number of face bolts has been set to 12. Presence of head plates was achieved by a rigid connection between the frontal bolt nodes and a shotcrete layer. Finally, no pre-stressing force was applied.

Table 2.5: Input parameters of the face bolts

Property	Symbol	Value	Unit
Young's modulus	E_{an}	45000	[MPa]
Unit weight	γ	25	[kN/m ³]
Cross sectional area	A	0.00157	[m ²]
Grout cohesive strength	c_g	200	[kPa]
Tensile strength	F_t	250	[kN]
Grout stiffness	k_g	17.5	[MPa]
Grout perimeter	p_g	0.1	[m]
Length	L_a	12	[m]
Number of bolts	-	12	[-]

2.3 Modelling sequence

As already mentioned, the objective of this thesis was to compare different shapes of the tunnel face. Thus, an additional parameter r_s was developed to characterize the shape of the face. Figure 2.3 shows the schema of a tunnel excavation with a spherical face. The arch (solid pink line) represents the face contour. The parameter r_s describes the length from the arch center to the center of its base. In the later part of this work r_s is related to the tunnel radius R .

Numerical simulations were conducted according to the principles of the step-by-step method (Wittke, 1999). The idea was to perform multiple rounds of excavation until the face was in a sufficient distance from the model edges. Thus, the influence of the artificial boundaries could be reduced.

The round length was set to 1 m. State of equilibrium was described in terms of a mechanical ratio. This value describes the relation between the out-of-balance force and the average mechanical force. The ratio was varied between 10^{-5} and 10^{-6} . However, it turned out that it had a low impact on the results. For example, with a ratio of 10^{-6} the face longitudinal displacement increased by only 5%. Moreover, the course of stresses obtained with both ratios was almost identical. Related diagrams can be found in Appendix A. However, the lower ratio caused an increase of the computational time by a factor of three. As a result, the simulation required 22h. Therefore, the ratio of 10^{-5} was maintained for further calculations. Given the above, it proved to be a satisfying compromise between the accuracy of calculations and the computational time.

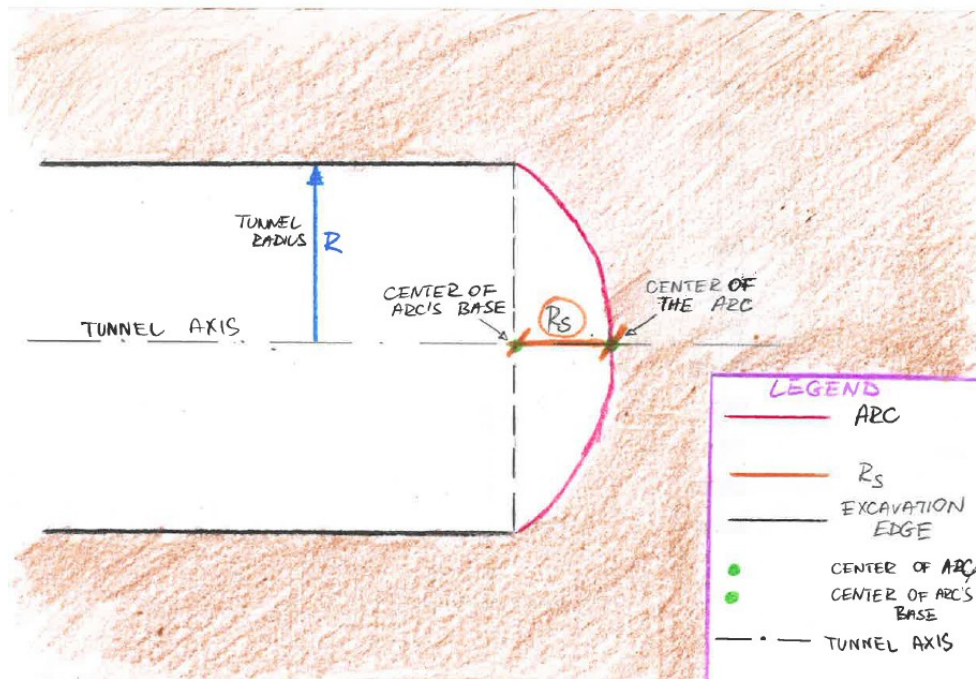


Figure 2.3: Description of the parameter r_s

In general, simulations have been divided into five groups:

- Failure mechanism (**group 0**)
- Unsupported tunnel (**group I**)
- Tunnel supported with lining (**group II**)
- Tunnel supported with lining and bolts (**group III**)
- Discussion (**group IV**)

Based on the group 0 it was attempted to illustrate the collapse mechanism with planar and spherical faces. Hence, only two models have been simulated. Material parameter set no. 2 was used to achieve large deformations of the tunnel. A uniform face support pressure has been applied until the face reached the position indicated by the cross section A-A. Then, the support pressure has been set to zero. As a result, a tunnel failure occurred.

The calculations carried out as a part of groups I, II have been divided into two subsections, namely a full face and a sequential excavation. Within the group III only full face excavations have been simulated. Four different face shapes are considered for the analysis of a full face excavation:

- $r_s = 0$ (**model 1**)
- $r_s = 0.2 * R$ (**model 2**)
- $r_s = 0.5 * R$ (**model 3**)
- $r_s = R$ (**model 4**)

The models are illustrated in Figure 2.4 and Figure 2.6.

Calculations with a sequential excavation have been classified into four groups:

- Top heading with vertical face - $r_s = 0$ (**model A**)
- Top heading with a core and vertical face - $r_s = 0$ (**model B**)
- Top heading with spherical face - $r_s = 0.2 * R$ (**model C**)
- Top heading with a core and spherical face - $r_s = 0.5 * R$ (**model D**)

Figure 2.5 and Figure 2.7 show the detailed geometries of those models. The reader is asked to remember the naming convention presented above. In order to avoid confusion, in the later part of this work only underlined, bold typed terms (e.g. model 1, model B) will be used.

The cross section of the sequential excavation was divided into a top heading and an invert. Additionally, two models contained a supporting core. As such, the dimensions concerning tunnel face, invert and the core have been summarized in Table 2.6. Values given in the brackets refer to the tunnel radius R.

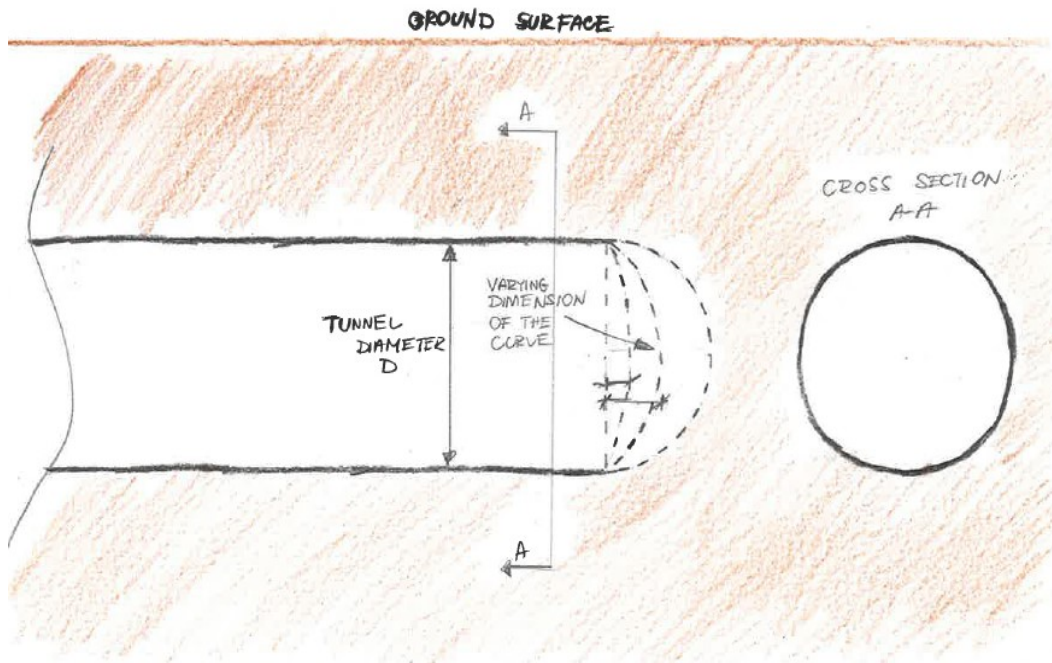


Figure 2.4: Unsupported full face excavation with a varying parameter r_s

The calculation of the primary stress state was the first step of each simulation. The gravitational load of the overlaying zones determined the value of vertical stresses. Horizontal stress was obtained by multiplying vertical stress by an earth pressure coefficient at rest. An empirical formula developed by Jaky (1944) and given in Eq. (2.1) provided an estimation of K_0 .

$$K_0 = 1 - \sin \varphi \tag{2.1}$$

Accordingly, $K_0 = 0.66$ was assumed. Once the primary state was calculated, element displacements and velocities were set to zero.

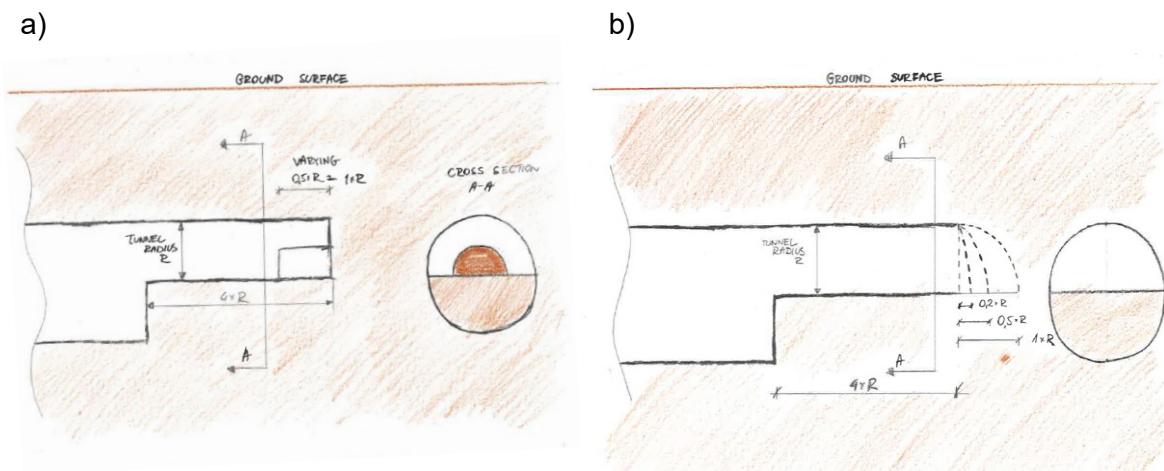


Figure 2.5: Unsupported sequential excavation: a) With supporting core and vertical face; b) Without core but with varying parameter r_s

Table 2.6: The dimensions of the excavation parts valid for a sequential excavation (e.g. models A, B, C and D)

Part of the cross section	Dimension along the axis	Value
Top heading	z-axis	5 m (R)
Invert	z-axis	5 m (R)
Invert	y-axis	10 m (2R)
Supporting core	z-axis	2.5 m (0.5R)
Supporting core	y-axis	2.5 m (0.5R)

The initial excavation sequence for groups II and III was the same as for an unlined tunnel. Yet, the removal of zones was followed by the application of shotcrete. The length of the support ring, like the unsupported length, was equal to 1 m. Figure 2.6 presents the models of a full face excavation with face bolts.

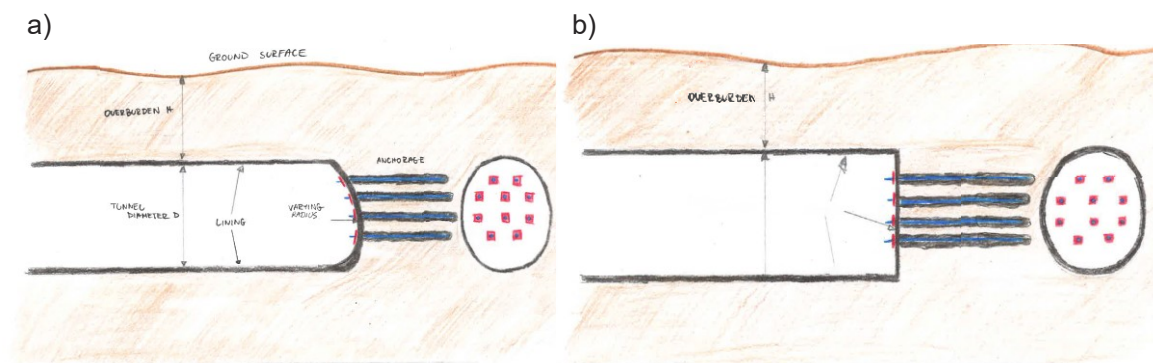


Figure 2.6: Supported full face excavation: a) Planar face; b) Spherical face

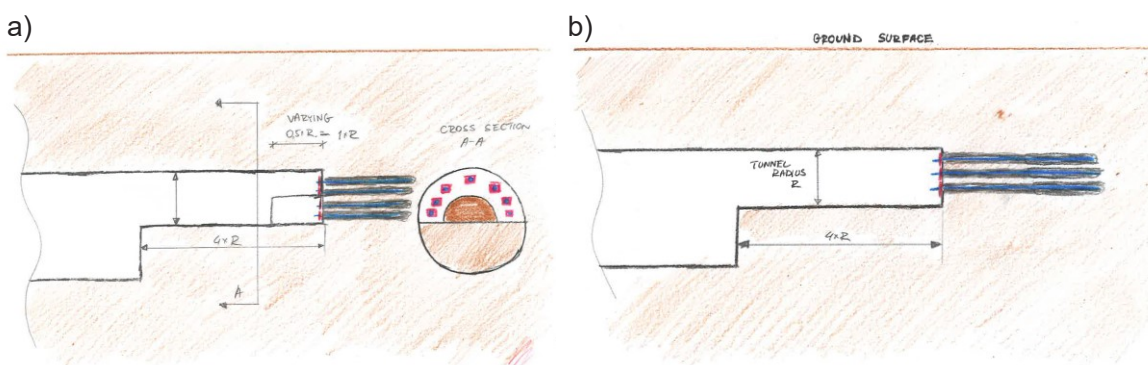
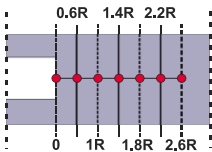
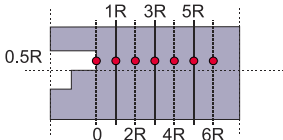
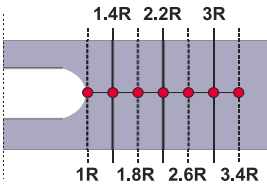
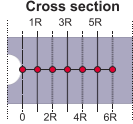
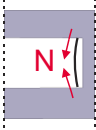
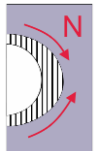
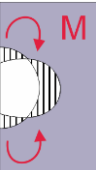


Figure 2.7: Supported sequential excavation: a) With supporting core; b) Without supporting core

2.4 Data analysis

The results were analysed at several control points. The symbols summed in Table 2.7 indicate the measured resultant (e.g. stress, internal force in support) as well as the location of the point.

Table 2.7: Control points

Description	Symbol
Normalized stress in the centre of a full face excavation. Horizontal axis shows a normalised distance ahead of the face in the longitudinal direction	
Normalized stress in the centre of a top heading excavation. Horizontal axis presents a normalised distance ahead of the face in the longitudinal direction	
Vertical stresses ahead of the face in [MPa]. Horizontal axis presents the value of stress, while vertical axis refers to the depth in [m]. Different line patterns refer to the distance ahead of the face	
Stresses ahead of the face in [MPa]. Vertical axis presents the value of stress, while horizontal axis refers to the distance from the tunnel centreline.	
Normal force in the lining at the face in [kN]	
Axial force in the support behind the face. Vertical axis presents the normal force in [kN]. Radial values points out the position on the ring	
Bending moment in the support. Vertical axis refers to the bending moment in [kNm]. Radial values indicate the position on the ring	

2.5 Model validation

2.5.1 Secondary stress state

A plausibility check was carried out in order to establish if the developed script is functioning correctly. Series of runs was performed using a slice of the chosen mesh. The length of the slice along the y-axis accounted to one round length. The author compared the numerically obtained stresses with the closed-form solution of Feder & Arwanitakis (1976). In addition, analytical solution derived by Kolymbas (1998) was utilized to validate the stresses ahead of the face. However, in the second test the limitations of the solution required an assumption of a hydrostatic stress state.

Figure 2.8 presents the comparison of radial and tangential stresses at the tunnel sidewall. Secondary stresses (vertical axis) are plotted against the normalized distance from the tunnel centreline (horizontal axis). Firstly, both solutions suggest the existence of a plastic zone around the excavation. Notice that the peak tangential stress obtained by the closed-form solution is approximately 10% higher than the result yielded with *FLAC*^{3D}. Furthermore, the location of the maximum tangential stress is slightly shifted. In the remaining course of stresses one can observe a constant difference in the values.

There are several possible explanation of the fact that stress states are not coherent. Firstly, Itasca (2017) states that the fixed model boundaries are responsible for stresses to be underestimated. Secondly, the difference may be caused by an assumption of a constant stress state by the solution of Feder & Arwanitakis (1976). Especially in case of shallow tunnels, this assumption may be incorrect. The reason for that is a relative increase of stresses with depth. To be specific, Table 2.8 shows the stress state at the level of the crown and invert. As the data points out, the change of stresses between the crown and the invert amounts to 50% of the stress state at the crown. Finally, the model width may be too short. The closed-form solution of Feder & Arwanitakis (1976) yields the initial stress state only 12R away from the tunnel centreline. However, numerical model with a comparable width would either cause an increase of the computational time or require a coarser mesh discretization. This was not desired. Furthermore, the accuracy of the results obtained in the longitudinal direction was of primary interest.

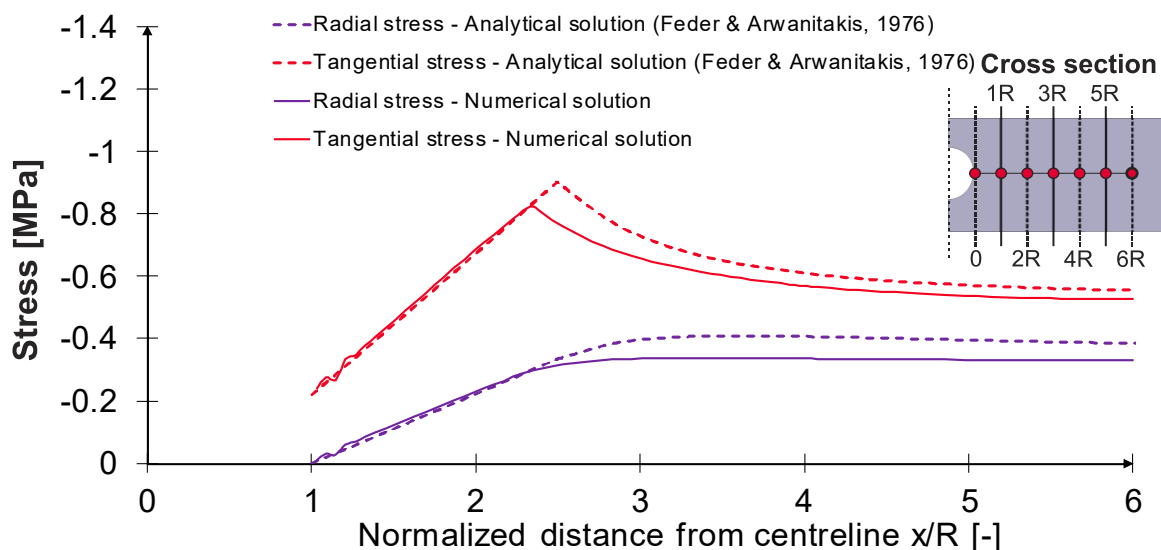


Figure 2.8: Comparison of the secondary stress state yielded with *FLAC^{3D}* and according to Feder & Arwanitakis (1976)

Table 2.8: Stress state at the level of tunnel crown and invert

	Stress at the crown level	Stress at the invert level	Difference (related to the stress at the crown)	
	[MPa]	[MPa]	[MPa]	[%]
σ_z	0.43	0.65	0.22	50%
σ_y	0.29	0.43	0.14	50%

Finally, Figure 2.9 illustrates the comparison of secondary stress states ahead of the face. The solid lines refer to the stresses obtained numerically, whereas the dashed lines present the results of the closed-form solution derived by Kolymbas (1998). The maximum numerical value of tangential stresses matches the results obtained with the analytical solution. Nevertheless, one can observe an offset between the analytical and numerical results. The model was unable to yield minimum radial stress at the tunnel contour. This indicated that the chosen mesh was too coarse. Thus, an additional refinement along the tunnel axis was necessary.

In order to check the plausibility of the obtained deformations further calculation with a finite element software was conducted. The results yielded by FE software (Rocscience: RS2, 2017) and FDM were in good agreement (see Appendix B). Therefore, the mesh was maintained for further calculations.

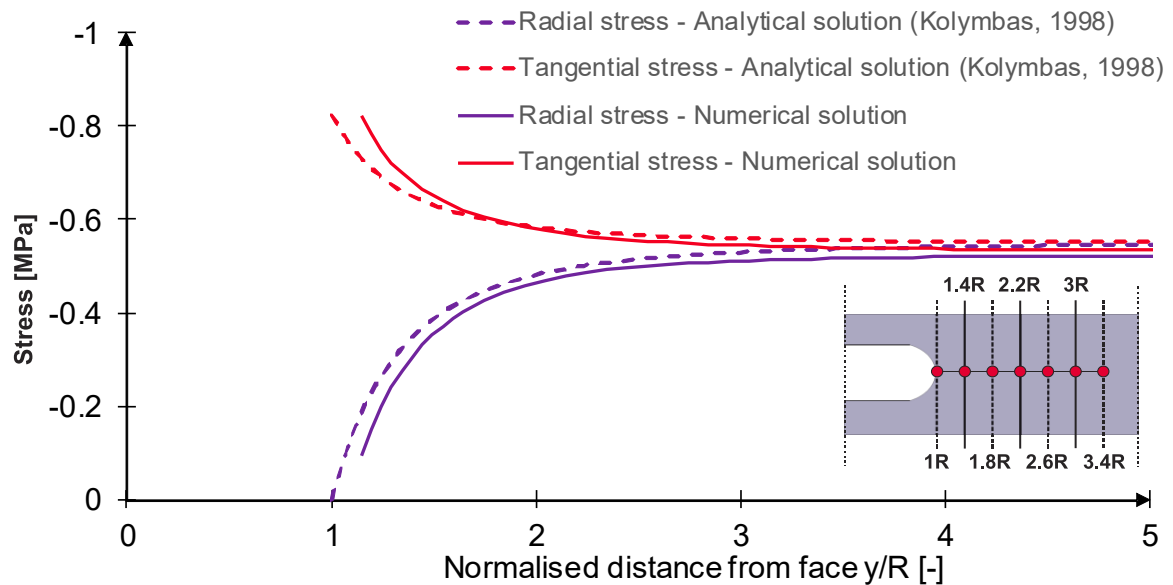


Figure 2.9: Comparison of the secondary stress state ahead of the face yielded with *FLAC^{3D}* and according to Kolymbas (1998)

2.5.2 Stress resultants in the lining

A series of tests has been performed in order to investigate the influence of the constitutive model on the lining behaviour. As such, the results of analytical solutions of Einstein & Schwartz (1979) and Ahrens et al. (1982) were used to validate the numerical results. The diagrams of internal forces can be found in Figure 2.10. The values have been plotted against the radial coordinate. Figure 2.10a presents the course of normal forces, whereas Figure 2.10b refers to the bending moments. In general, the solution of Ahrens et al. (1982) yielded the highest internal forces. The results obtained with the solution of Einstein & Schwartz (1979) shows a satisfying agreement with the numerical results with the MC. On the contrary, the internal forces calculated with the Plastic Hardening model are significantly lower.

The difference between the results obtained with the Mohr-Coulomb and the Plastic Hardening may be caused by an assumption of a constant soil stiffness in the MC. As such, the virgin loading stiffness and unloading/reloading stiffness are equal. In reality, however, stiffness parameters are stress dependant. In fact, stiffness during the unloading is 2-3 times higher than during the primary loading. Hence, tunnel lining calculated with the Plastic Hardening is subjected to lower loads. This can be seen especially in the plot of the bending moments (see Figure 2.10b).

Note that with both numerical results the axial forces in the invert are higher than at the crown. Do et al. (2013) reported similar results. The cause seems to be an increase of loads over the tunnel height. Notably, it plays a crucial role for shallow tunnels under a low stress state. An increased load acting on the invert causes an increase of the internal forces. On the contrary, both analytical solutions assume that the load acting on the lining is constant. Therefore, values at the crown and in the invert are equal. Given the above, it was chosen to conduct the initial calculations with the MC. Although the ground behaviour is not realistically predicted, the Mohr-Coulomb provides a conservative approximation of the lining forces.

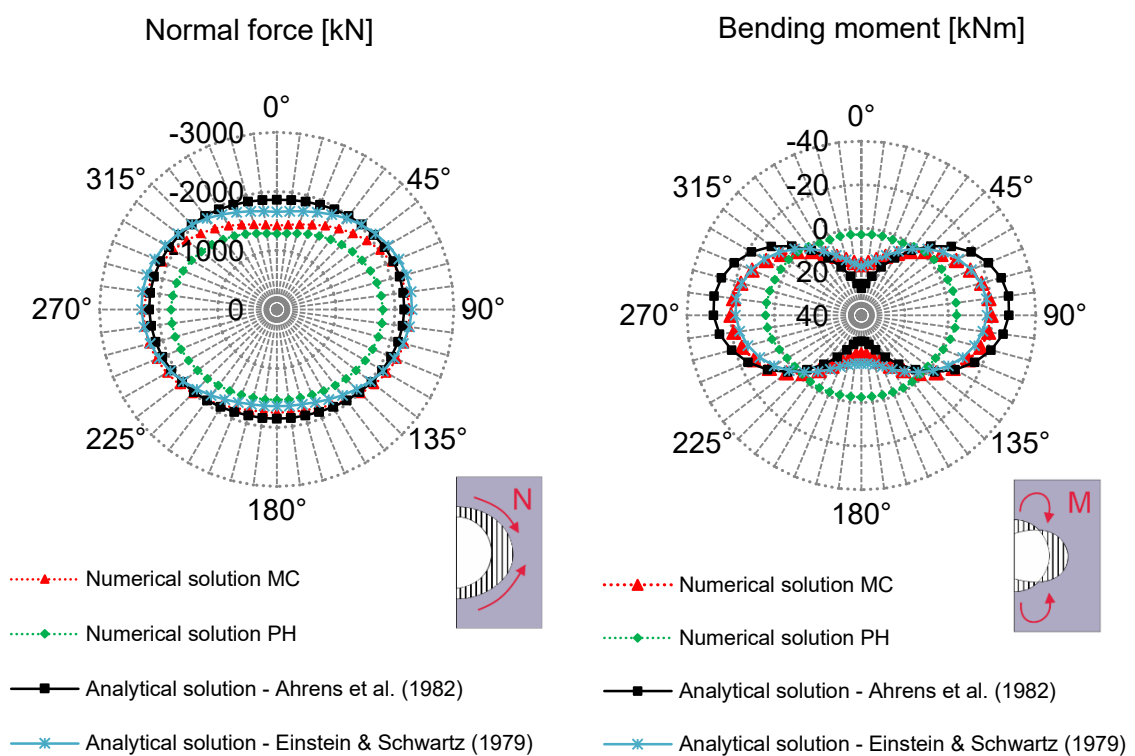


Figure 2.10: Comparison of internal forces in the lining yielded with $FLAC^{3D}$ and according to the analytical solutions of Einstein & Schwartz (1979) and Ahrens et al. (1982): a) Normal forces; b) Bending moments

3 Results

3.1 Failure mechanism

The simulations in the following subsection have been performed with the parameter set no. 2. Figure 3.1b and Figure 3.2b present the vertical stresses ahead of the face. Stresses have been plotted at different distances to the face to investigate the formation of a load-bearing arch. The solid lines represent the primary vertical stress, whereas the horizontal dashed lines refer to the levels of the crown and invert.

Turning our attention to the vertical face, a notable increase of vertical stresses takes place between the positions $1.4R$ and $2.6R$ ahead of the face. However, in case of a spherical face an equivalent increase of stresses occurs between the positions $1.8R$ and $3R$. Those stress concentrations suggest a formation of the load-bearing arch. Though, as previously anticipated by Kusumoto et al. (2013) and Shinji et al. (2004), with a spherical face the arching appears closer to the excavation contour than with a vertical heading.

Apart from the change of the arch positions, different collapse mechanisms were encountered (see Figure 3.1a and Figure 3.2a). The failure contours have been highlighted with a dashed line. It can be observed that a planar face experiences a semi-circular failure. A similar shape was already proposed by Krause (1987) and later confirmed by Schubert & Schweiger (2004). The prism extends to $1.5R$ above the tunnel crown, whereas the wedge ahead of the face expands horizontally by $1R$. Turning our attention to a spherical face one can observe a chimney-shaped failure. While the volume of the wedge is significantly lower than with the vertical face, the prism extends to $4R$ above the crown. In case of a shallow tunnel the prism may reach the ground surface. The most likely reason of this behaviour is a greater unsupported length. Remember that with the planar face the unsupported span was equal to $0.2R$, whereas with the spherical face it can be assumed as r_s (i.e. R).

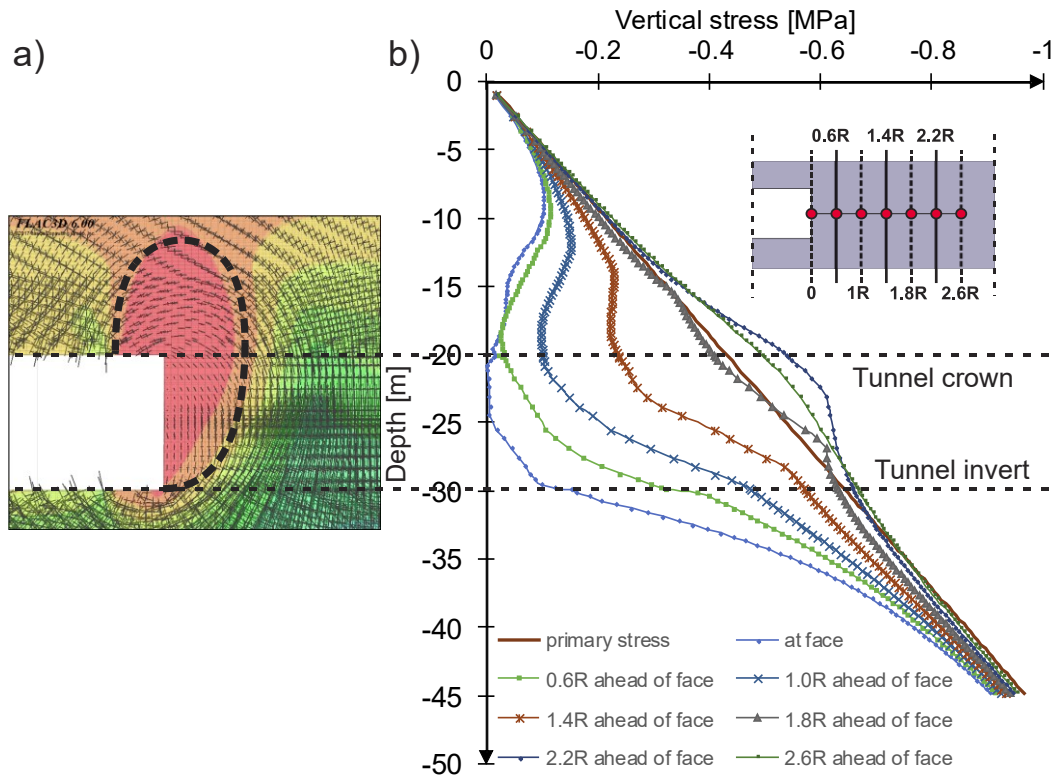


Figure 3.1: a) Failure mechanism with a planar face; b) Vertical stresses as a function of depth for different positions ahead of the face

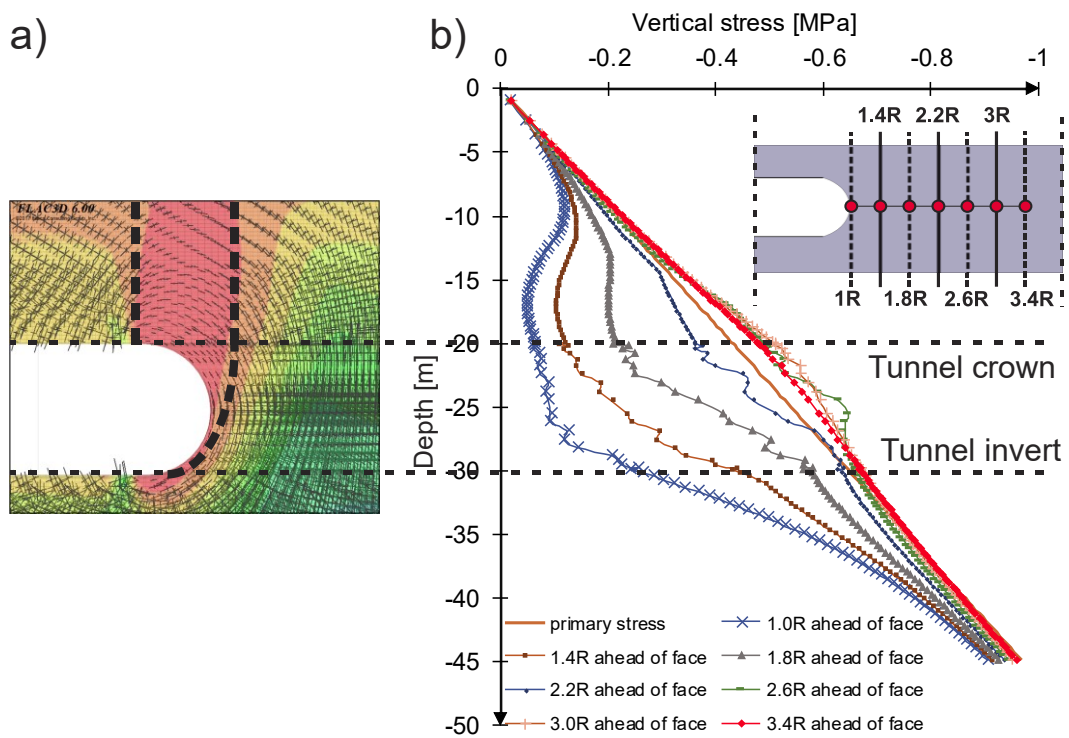


Figure 3.2: a) Failure mechanism with a spherical face; b) Vertical stresses as a function of depth for different positions ahead of the face

3.2 Unsupported tunnel

The simulations in the next two subsections have been performed with the parameter set no. 1.

3.2.1 Full face excavation

Figure 3.3 shows the comparison of secondary stresses for an unsupported tunnel. For each case, the left side of the figure shows the distribution of radial stresses on the vertical plane (y - z plane), whereas the right side presents the stress state as a function of the face distance. The legend displayed in Figure 3.3e is valid also for Figures 3.7, 3.10 and 3.17. Clearly, the stress relaxation occurring ahead of the face can be seen. Keep in mind that the values on the vertical axis are the normalised stresses. The horizontal axis refers to a longitudinal distance from the face.

The stress relaxation (elements marked with red) of a planar face is generally much more severe than with a spherical face. As the r_s rises, tangential stresses at the face increase. Similarly, the gradients of radial stresses increase as the r_s rises. Therefore, the elements near the excavation perimeter increase their participation in the stress redistribution. As a result, with spherical face the primary stress state is achieved closer to the excavation contour than with a planar face.

The deformation of the tunnel is presented in Figure 3.4. Model 1 and 2 are shown in the upper row while model 3 and 4 are placed in the lower level. The red contours indicate face deformations. A positive value of displacement means that the ground moves towards the excavation. Note that the horizontal axis refers to the normalized distance from the face.

As expected, in all investigated cases the maximum longitudinal deformation occurs in the center of the face (Cantieni, 2011). The displacements are quite different, ranging from 42 mm with the vertical face to 23 mm with the spherical one. As this case clearly demonstrates, the rise of the r_s leads to a reduction of longitudinal displacements at the face. In fact, with the model 4 one can observe a decrease of horizontal movements by almost 50%. Furthermore, the face deformations are reduced by 17% and 36% for cases with $r_s = 0.2R$ and $r_s = 0.5R$, respectively. Finally, it has been shown that the shape of a face influences the deformations in the tunnel crown and invert only marginally.

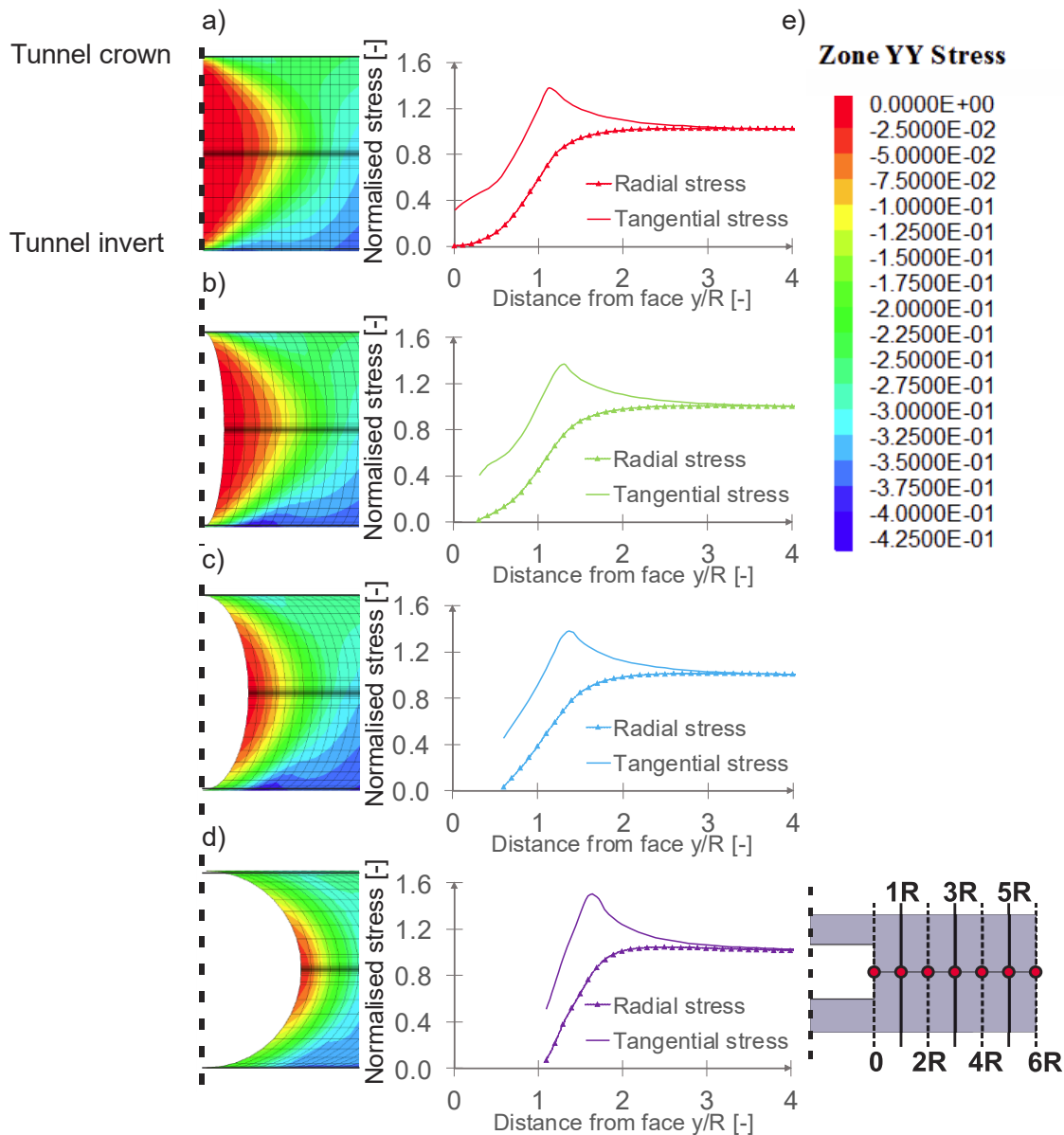


Figure 3.3: Secondary stress state at the face as a function of face distance. Unsupported full face excavation: a) Model 1; b) Model 2; c) Model 3; d) Model 4; e) Legend

The displacement plots give a first insight into the possible extent of a failure zone. Those are shown in Figure 3.5. The horizontal lines placed in the lower part of each graph refer to the length of a plastic zone. It is quite apparent that the largest failure zone develops ahead of the vertical face. As presented in Figure 3.5a, it extends to $1.2R$ ahead of the face. The elements in the centre of the cross section fail under tension, while the remaining zones exhibit a shear failure. Note that with a higher r_s the volume of the plastic zone decreases. In fact, with the model D only zones within $0.5R$ from the face deform plastically (Figure 3.5d). Furthermore, tensional failure does not appear. While for the vertical face the greatest plastic radius develops in the middle of the cross section, the spherical face experiences a uniform distribution of plastic zones.

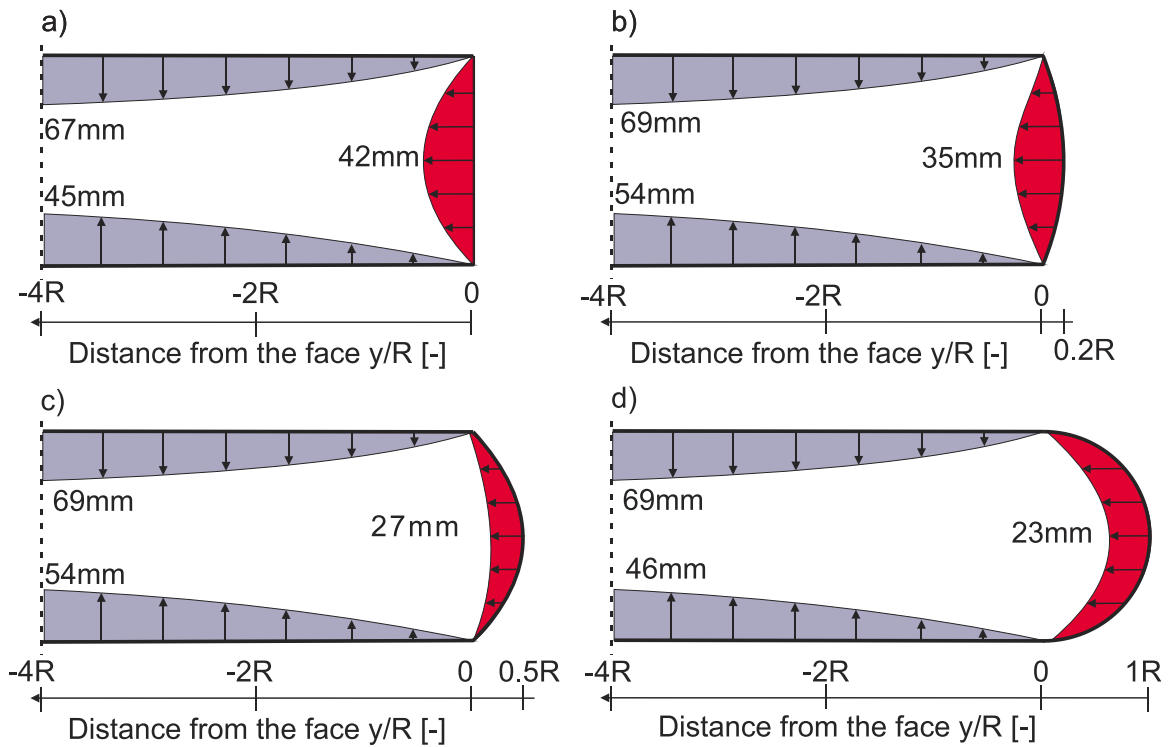


Figure 3.4: State of deformation at the face. Unsupported full face excavation: a) Model 1; b) Model 2; c) Model 3; d) Model 4

A further comparison of plastic zones is presented in Figure 3.6. This time, however, the plastic radius is shown as a function of the face distance on the horizontal plane (x - y plane). The horizontal axis shows the distance along the tunnel centreline, whereas the vertical axis indicates the size of the plastic zone. Finally, the blue solid line refers to the tunnel contour. Figure 3.6 is quite revealing in a number of important ways. At first, plastic zone further than $2R$ behind the face is comparable in all investigated cases, regardless of the r_s . However, the extent of plastification ahead of the face is different. For example, note a significant increase of the failure zone between the positions 0 and $1R$ with the model 4 (green line).

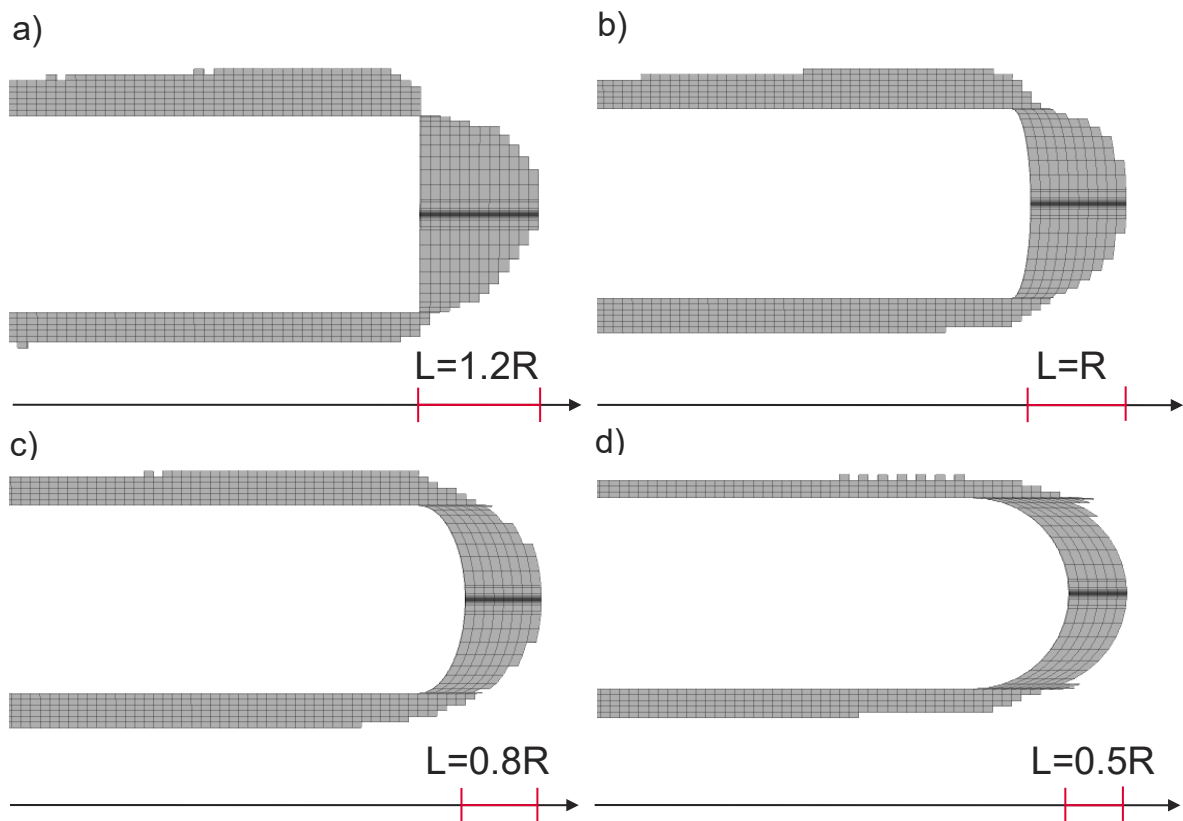


Figure 3.5: Plastic state at the face. Unsupported full face excavation: a) Model 1; b) Model 2; c) Model 3; d) Model 4

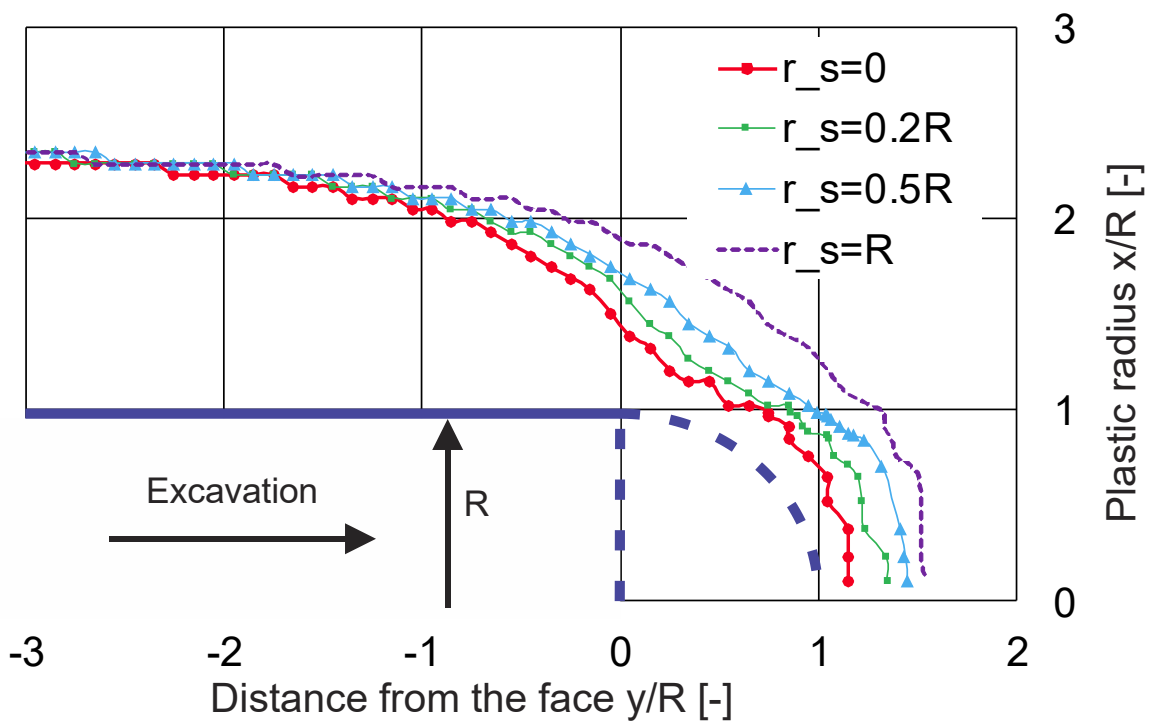


Figure 3.6: Plastic radius as a function of face distance. Unsupported full face excavation

3.2.2 Top heading excavation

Figure 3.7 compares the secondary stresses obtained with the sequential excavations. As before, the left side of each diagram shows the distribution of radial stresses, whereas the right side presents the stress state as a function of the face distance. The positive values on the horizontal axis indicate a position ahead of the face. Figure 3.7 is quite revealing in a number of ways. On one hand, the most severe relaxation occurs with the top heading excavation. This is illustrated in Figure 3.7a. On the other hand, the presence of a core leads to an increase of stresses at the face. The radial stress development with models B and D shows this clearly. This suggests that the core causes the load-bearing arch to form closer to the excavation perimeter. Finally, we turn our attention to the spherical face. However, model 3 shows that the spherical face does not influence the ground behaviour significantly. The only difference is a slightly higher tangential stress and the gradient of radial stresses.

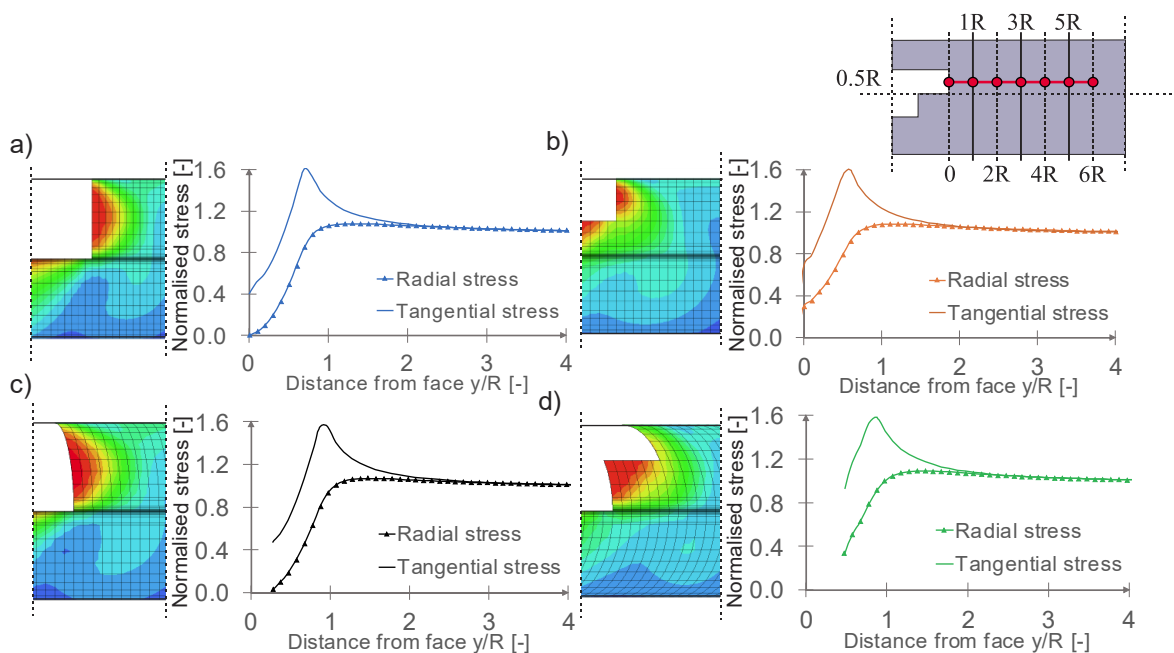


Figure 3.7: Secondary stress state at the face as a function of face distance. Unsupported sequential excavation: a) Model A; b) Model B; c) Model C; d) Model D

Papakonstantinou (2008) in his doctoral thesis already reported the effects of a sequential excavation on the tunnel deformations. Nevertheless, Figure 3.8 shows the deformational state at the face with a sequential excavation. Interestingly, presented results differ in a number of important ways. Firstly, the highest deformation takes place with the top heading excavation. Secondly, as already reported by Kusumoto et al (2013), the full face excavation with a spherical face yielded lower face deformation than the top heading

excavation (model A). Interestingly, the longitudinal displacements obtained with the models B and C are very similar. To be specific, model B yielded a maximum horizontal displacement of 25 mm, whereas model C almost 27 mm. While both models were able to reduce the deformations notably, none of them achieved the results comparable with the model D. The maximum face displacement was only 13 mm. However, low deformations at the face were accompanied by a horizontal displacement of the core of 40 mm.

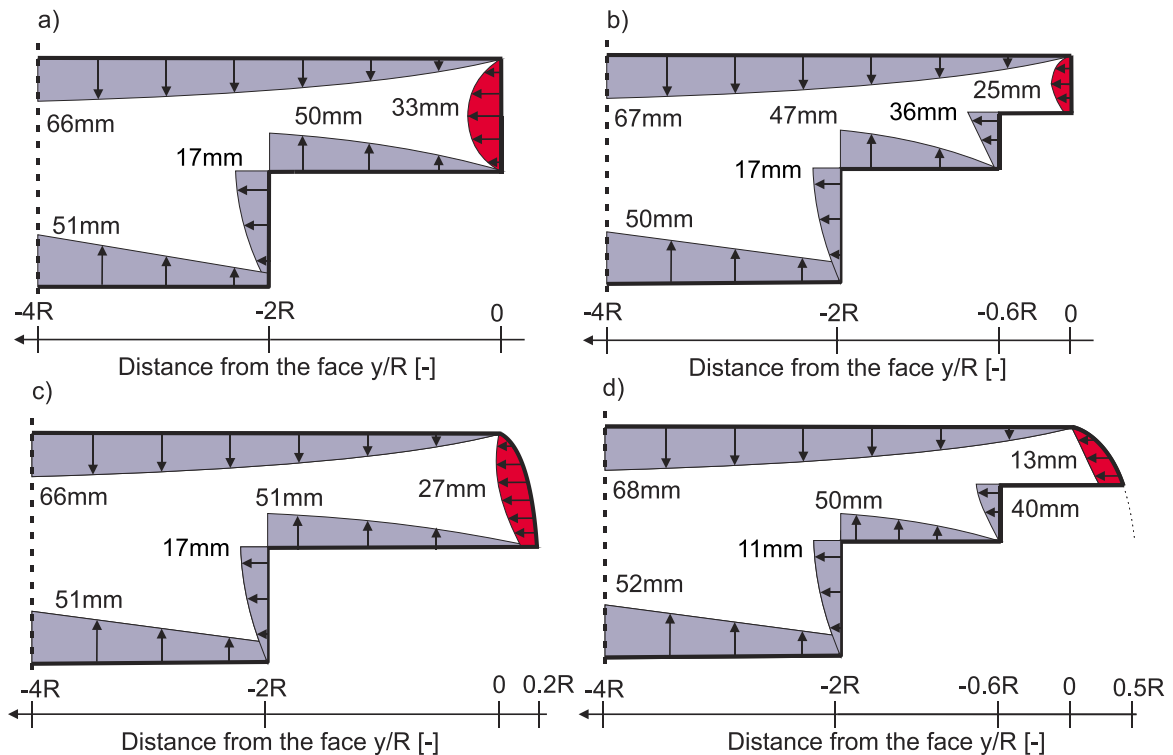


Figure 3.8: Comparison of face displacement. Unsupported sequential excavation: a) Model A; b) Model B; c) Model C; d) Model D

The final part of this section deals with the comparison of plastic states. Firstly, note that the presence of a core significantly reduced the length of the failure zone. This can be seen in Figure 3.9b and in Figure 3.9d. Generally, the geometry of failure zone matched the findings of Sternath & Baumann (1997). While the smallest plastic zone occurred with the model D, the greatest plastification developed with the model A. Again, a comparable behaviour was observed with the models B and C. The length of the plastic zone ranged between $0.4R$ and $1R$ for model D and A, respectively. In addition, note a significant decrease of the plastic radius with the spherical face (Figure 3.9c). Finally, the appearance of the plastic state in the core explains the large deformations illustrated in the displacement plots.

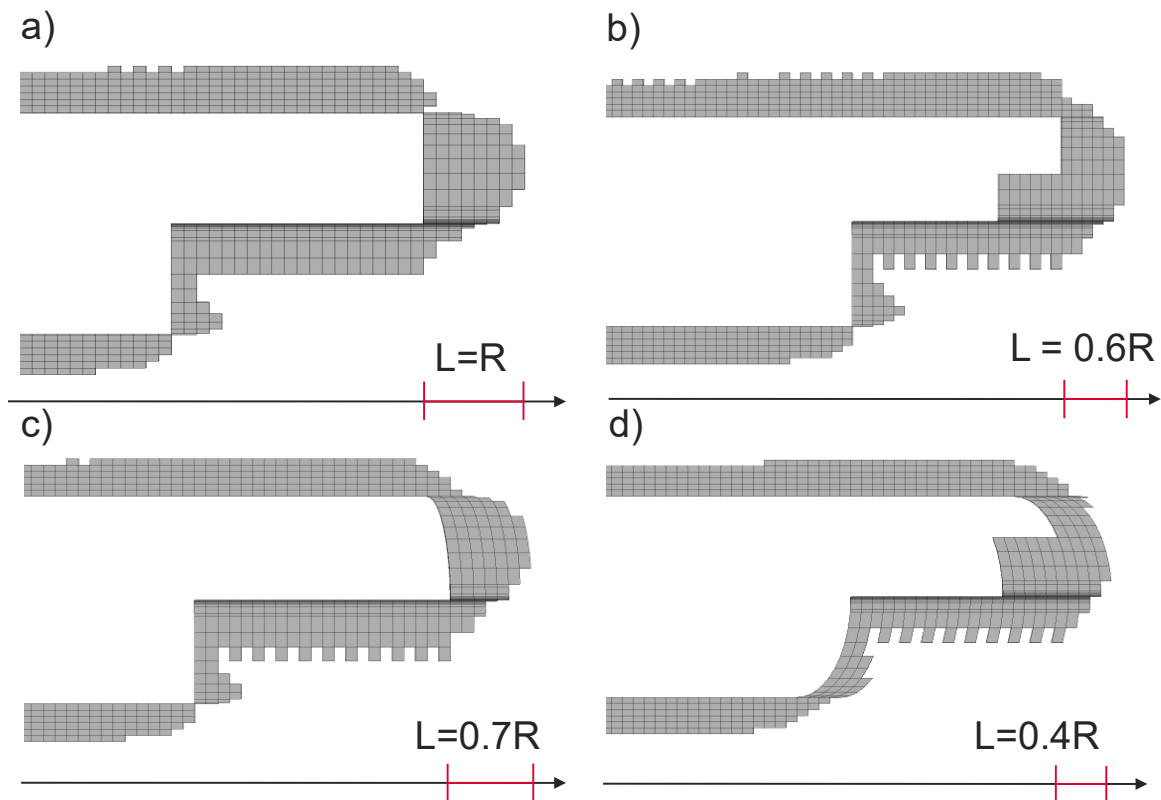


Figure 3.9: Plastic state at the face. Unsupported sequential excavation: a) Model A; b) Model B; c) Model C; d) Model D

3.3 Shotcrete lining

As in the subsection 3.2, the simulations in the following part were performed with the material set no. 1.

3.3.1 Full face excavation

The secondary stress state at the face of a supported tunnel is summarized in Figure 3.10. The results are shown in the same manner as in subsection 3.2. There are several important findings presented below. Firstly, even with the application of a lining, the vertical face experiences a significant relaxation. This means that the elements close to the excavation contour do not participate in the redistribution of stresses. However, as the parameter r_s increases, one can observe a notable increase of stresses at the excavation perimeter. In fact, with the chosen set of ground parameters, the spherical face (model 4) exhibits an elastic behaviour. Yet, from a global perspective the stress state does not change, regardless of the parameter r_s . It is important to understand that with the spherical face the zones where a large relaxation occurs are simply removed. The remaining course of stresses does not change. This is clearly seen by comparing Figure 3.10a and Figure

3.10d. Starting from 1R ahead of the face, the stress development is almost identical. Figure 3.11 presents a further support of these findings. The diagram shows the development of the vertical stresses at different positions ahead of the face. The legend illustrated on the left side is valid also for Figure 3.11b.

Figure 3.11a deals with a vertical heading ($r_s = 0$). A considerable stress reduction at the face is denoted by the dashed orange line. Stress concentrations develop first 1R ahead of the heading. Furthermore, the primary stress state is achieved at around 2R ahead of the face. Turning our attention to a spherical face ($r_s = R$), the stress concentrations occur at exactly same position, that is between 1R and 1.8R ahead of the face. Interestingly, the location of stress concentrations does not change, regardless of the shape of the face. While with the spherical face the load-bearing arch develops directly at the excavation perimeter, with a planar face the distance between the face and the arch is equal to 1R.

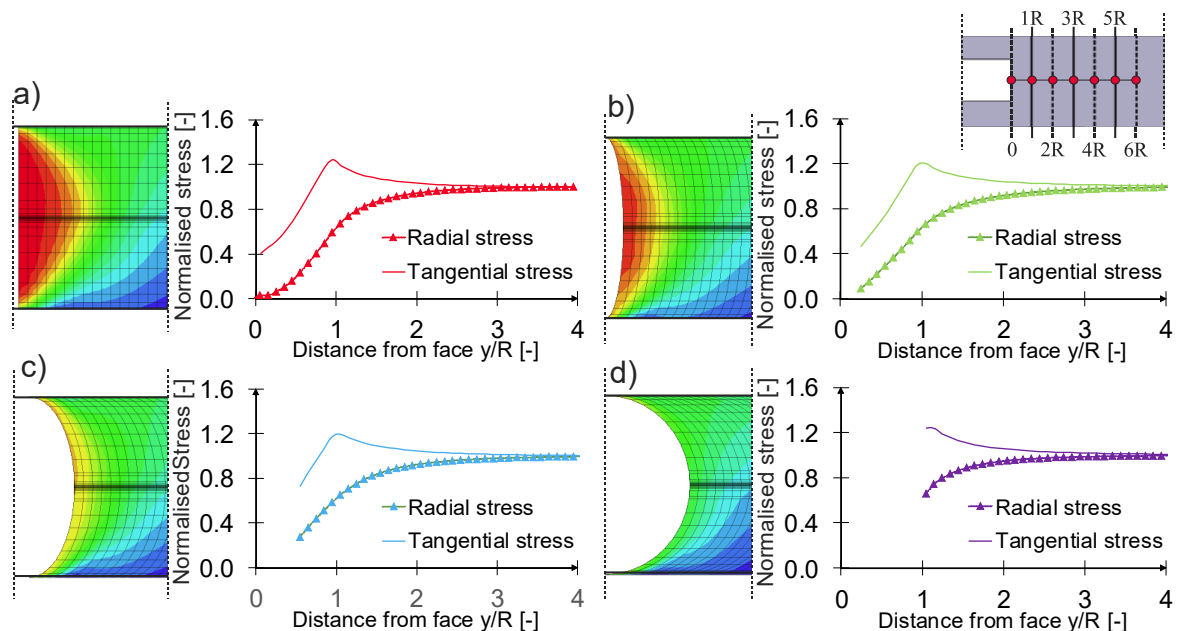


Figure 3.10: Secondary stress state at the face as a function of face distance. Supported full face excavation: a) Model 1; b) Model 2; c) Model 3; d) Model 4

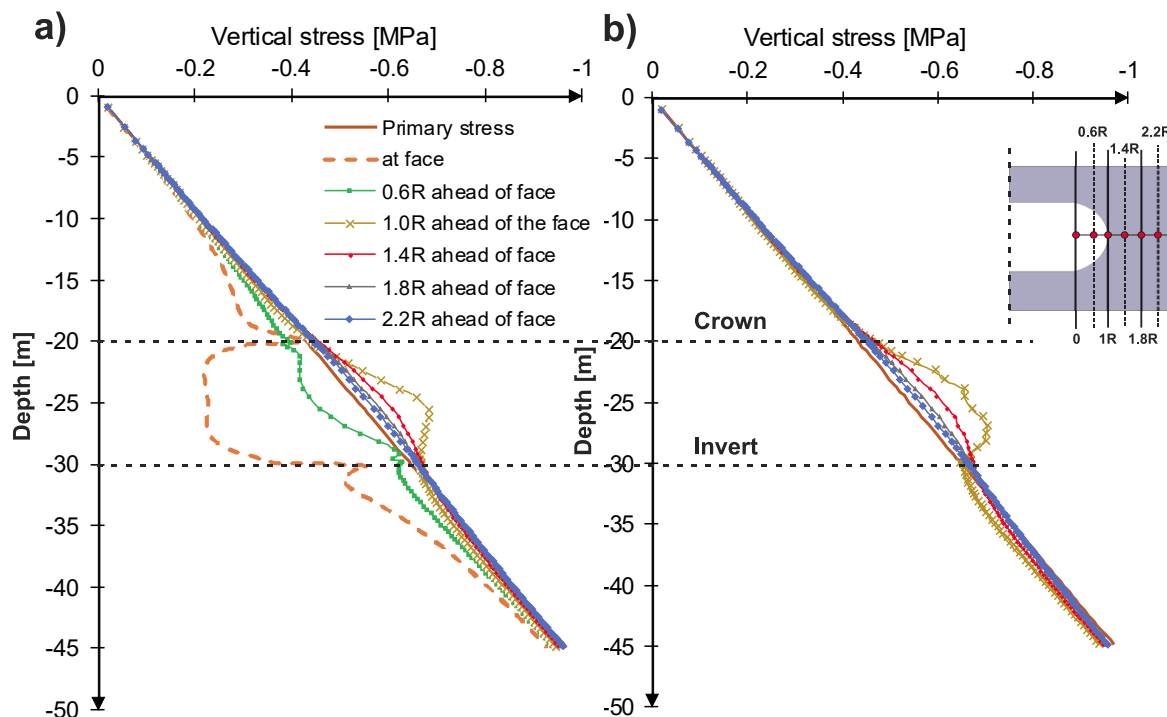


Figure 3.11: Vertical stresses as a function of the depth shown for different positions ahead of the face. Supported full face excavation: a) Vertical face; b) Spherical face

So far, this work dealt with stress and deformational states of the tunnel. In addition, the dimensions of plastic zones have been presented. As such, the next subsection deals with internal forces in the tunnel support. This includes the analysis of the normal forces in the lining at the face (see Figure 3.12) and in the tunnel wall (see Figure 3.13). In Figure 3.12 stress resultants obtained with different r_s are plotted against the distance to the face centreline. It shows that the normal force in the lining strongly depends on the heading shape. The maximum force is obtained with the model D. However, as the r_s decreases, the axial force in the lining decreases. In fact, normal force in the model A is only 18% of the normal force in the model D. This is understandable as the loading acts primarily perpendicular to the support.

Figure 3.13 illustrates internal forces in the lining at the wall. The resultants were obtained for the lining section placed one round length behind the face. Axial forces are plotted against the radial coordinate. Interestingly, an increase of parameter r_s causes the forces to decrease. The values in the sidewall ranged between 840kN and 670kN. In fact, the lowest force is obtained with the model D. Thus, it confirms the findings of Kusumoto et al. (2013). The author assumed that a spherical face causes a decrease of internal stresses in the tunnel lining. To be specific, Kusumoto et al. (2013) reported a reduction of stresses up to 34%. Amemiya et al. (2014) drawn similar conclusions.

There is at least one explanation related to these results. Firstly, in case of a spherical face, the crown displacement directly behind the face amounts to 60% of the final deformation. However, with the vertical face this value is equal to only 40%. It means that behind the spherical face only 40% of deformations are still expected. On the contrary, with the planar face 60% of final displacement are still to happen behind the face. It has been agreed that the tunnel displacements are the function of a stress release (Carranza-Torres & Fairhurst, 2000). The more pressure is dissipated, the less displacement occurs after tunnel support is applied. In other words, the more displacement occurs before the support application, the less load is later applied on the lining. Thus, model D yields the lowest internal forces in the support.

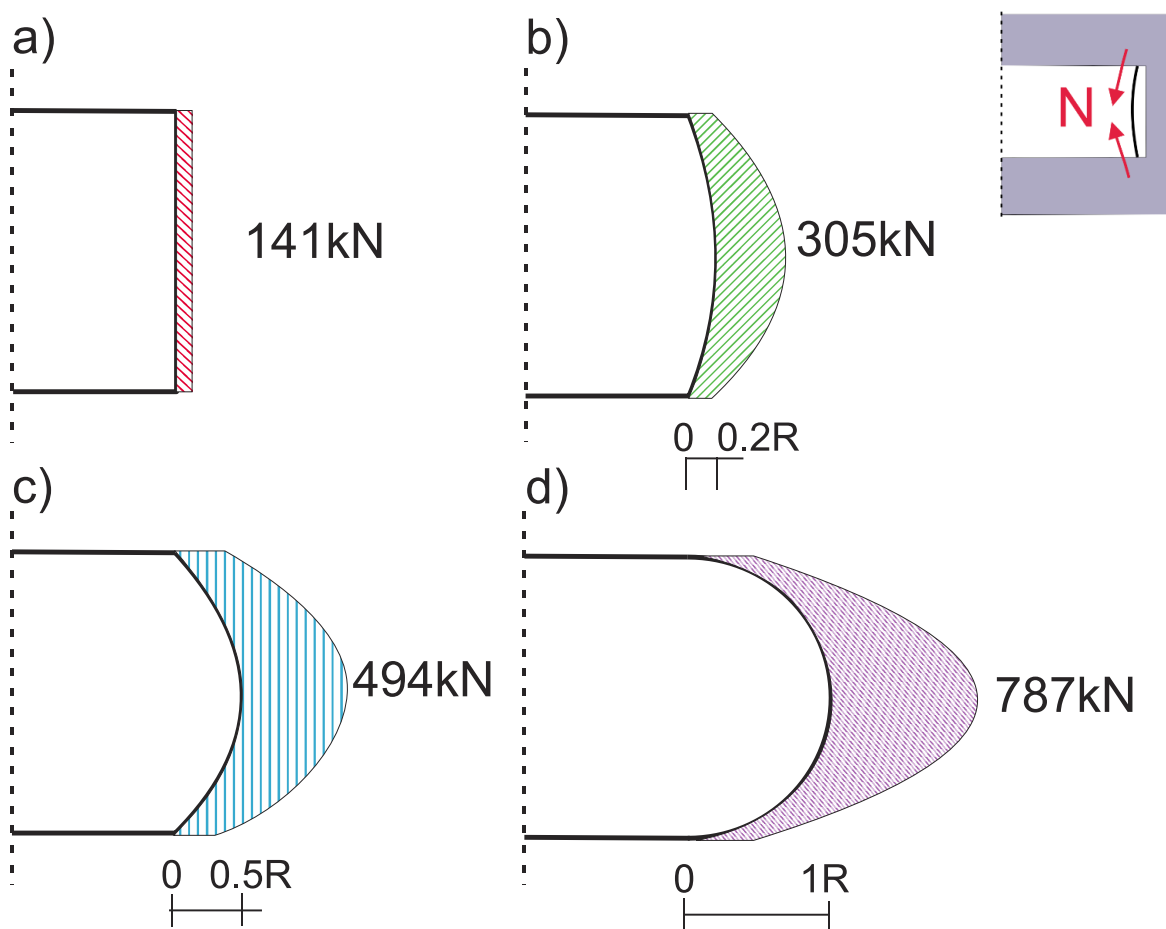


Figure 3.12: Internal forces in the face support. Supported full face excavation: a) Model 1; b) Model 2; c) Model 3; d) Model 4

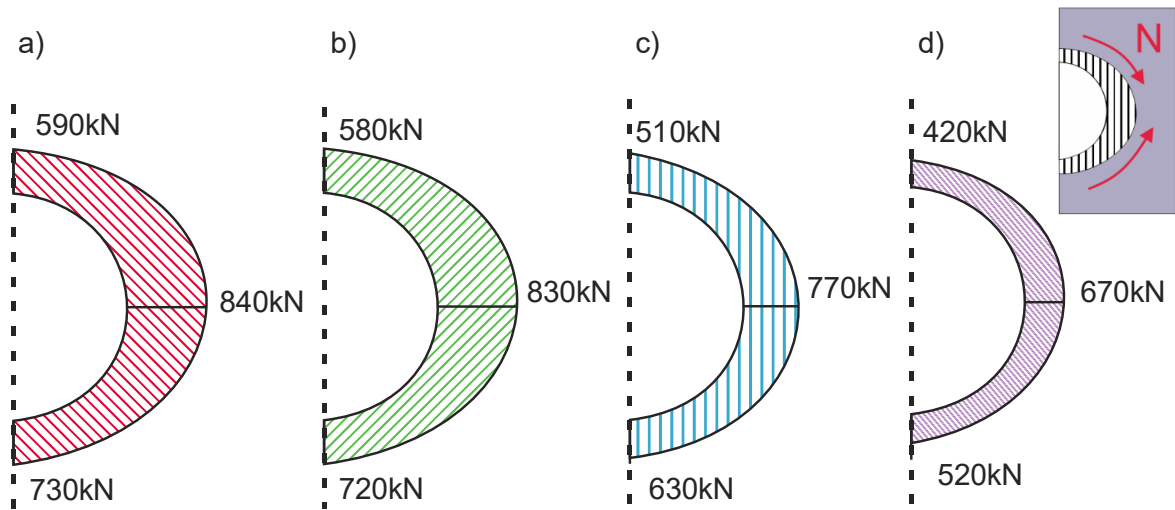


Figure 3.13: Internal forces in the support at the tunnel wall. Supported full face excavation: a) Model 1; b) Model 2; c) Model 3; d) Model 4

Figure 3.14 turns our attention to the ground displacements. Similar to the unsupported case, the highest deformation appears with the vertical face. While the maximum deflection of the vertical face exceeds 33 mm, the displacement of the spherical face reaches only 8 mm. In addition, a more uniform distribution of displacements is observed.

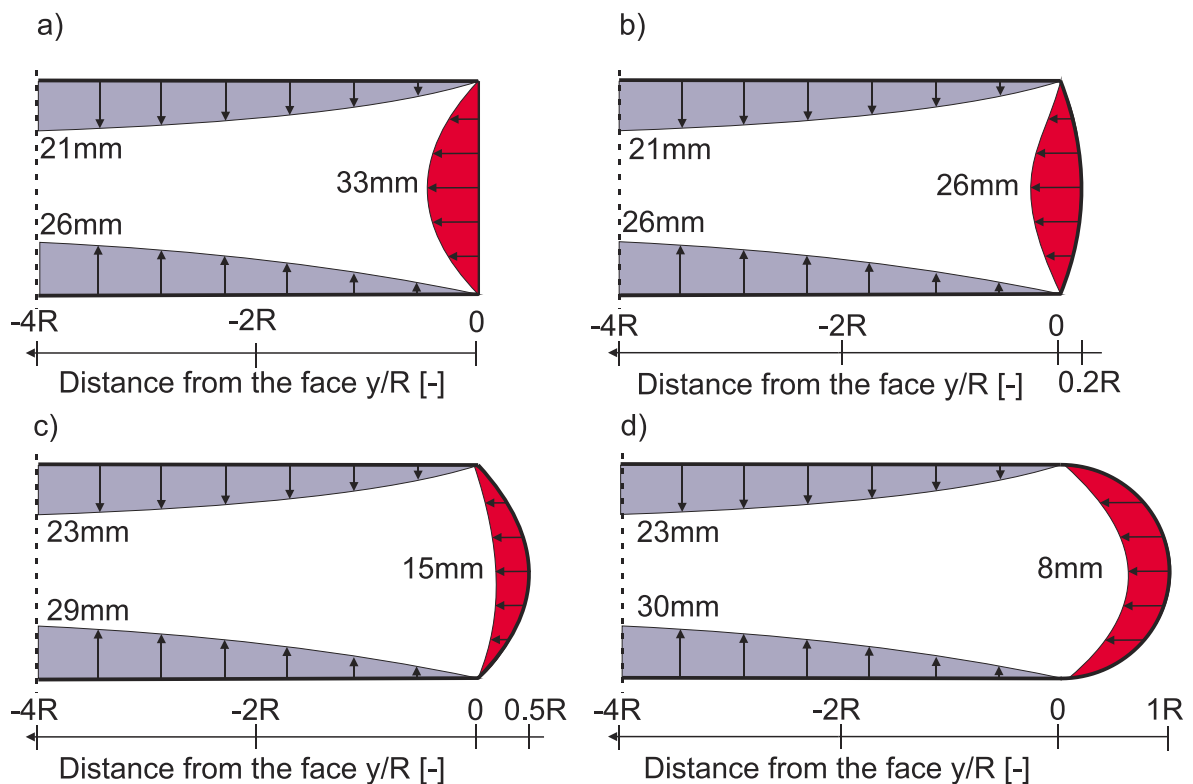


Figure 3.14: State of deformation at the face. Supported full face excavation: a) Model 1; b) Model 2; c) Model 3; d) Model 4

The displacement plots give a first insight into the extent of a failure zone ahead of the heading. A comparison of the plastic zones is shown in Figure 3.15. The plots show the extent of the plastic zone on the vertical plane (y-z plane). Note that despite the application of a support, the ground strength near the excavation contour is exceeded. As a result, plastic zones develop ahead of the face. The volume of the failure zone is generally much higher with a vertical face (Figure 3.15a) than with a spherical one (Figure 3.15d). While with the planar face the plastic zone extends to $1R$ ahead of the heading, with the spherical face only elements within the distance of $0.1R$ from the excavation perimeter exhibit plastic behaviour. Thus, the plastic radius is reduced by a factor of ten. A comparison of plastic zones on the horizontal plane can be found in Figure 3.16. The plastic zone has a comparable shape, regardless of the parameter r_s .

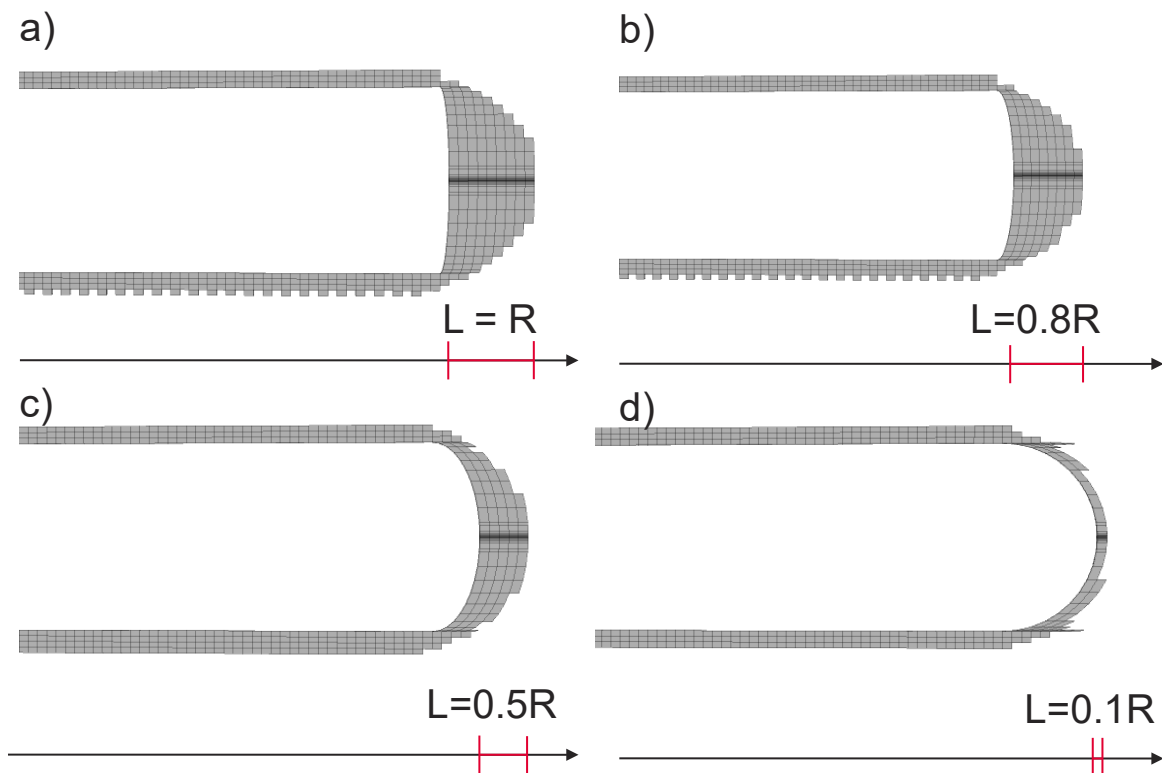


Figure 3.15: Plastic zone around the excavation. Supported full face excavation:
a) Model 1; b) Model 2; c) Model 3; d) Model 4

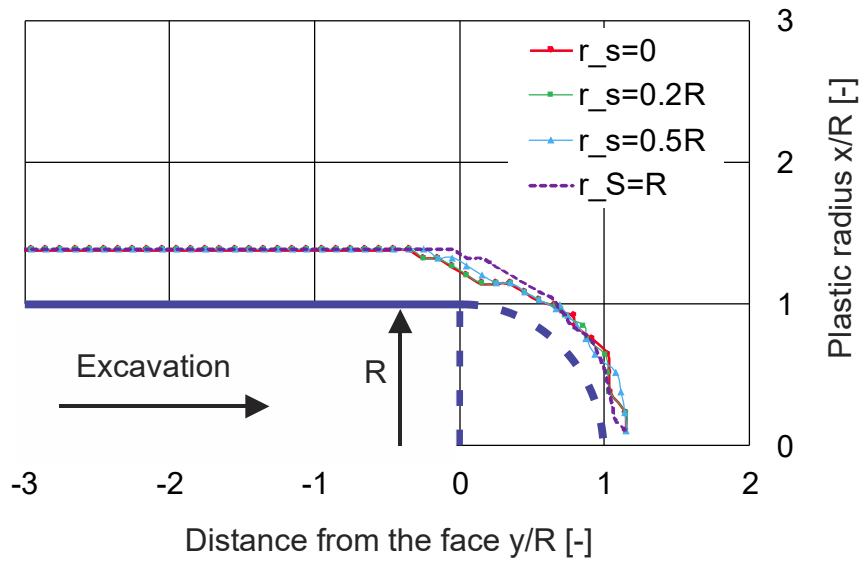


Figure 3.16: Comparison of the plastic radius. Supported full face excavation

3.3.2 Top heading

Finally, the results concerning a supported top heading excavation are presented. Figure 3.17 illustrates the secondary stress state ahead of the face. Despite the application of shotcrete, model A still exhibits a severe relaxation at the face. As before, the spherical face showed an increase of stresses at the excavation perimeter. Concerning the models with a supporting core, a careful reader will observe a notable increase of radial stresses at the face. This is illustrated in Figure 3.17b and Figure 3.17d.

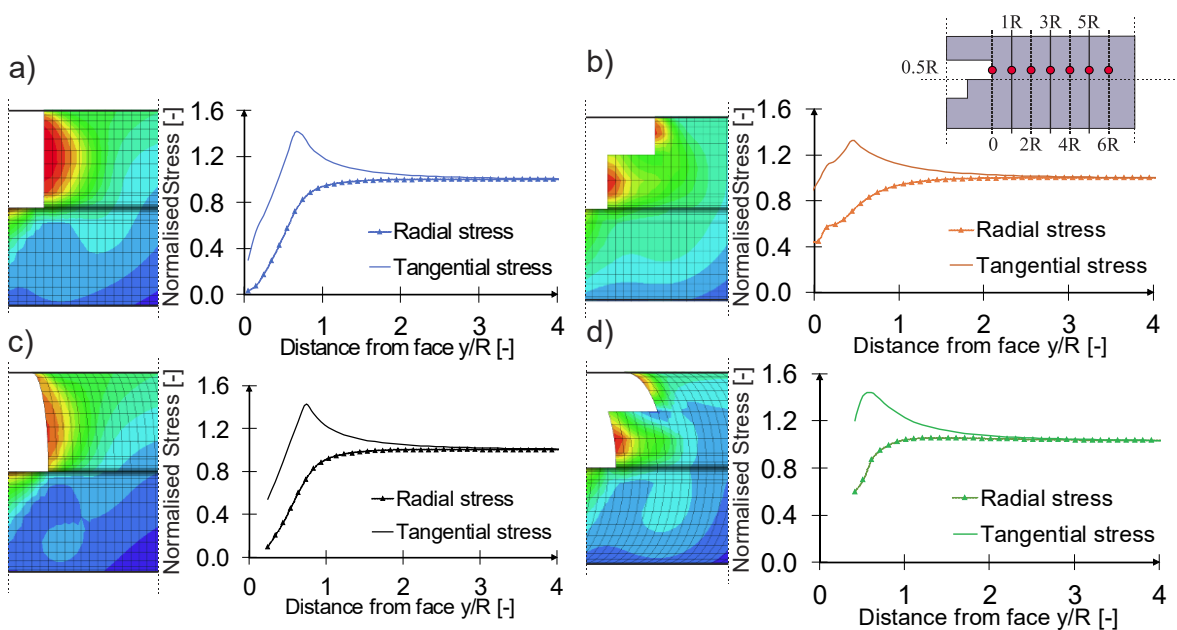


Figure 3.17: Secondary stress states as a function of face distance. Supported sequential excavation: a) Model A; b) Model B; c) Model C; d) Model D

Higher stresses at the excavation perimeter influence the deformations at the face. The plots of deformations can be found in Figure 3.18. As expected, the highest extrusion develops with the model A. (see Figure 3.18a). In this case, the maximum horizontal displacement at the face is equal to 27 mm. A notable displacement reduction occurred with models B (see Figure 3.18b) and C (see Figure 3.18c). While the model B experiences a face longitudinal displacement of 11 mm, model C yields 18 mm of horizontal movement. Finally, Figure 3.18d shows the model D where a spherical face and supporting core have been combined. As a result, the displacement of the heading as well as movement of the core have been further reduced. To be specific, the deformations of the face and the core were equal to 8 mm and 15 mm, respectively. What stands out for all the cases is a relatively large vertical deformation of the bench. As suggested previously, it is a drawback of a Mohr-Coulomb constitutive model.

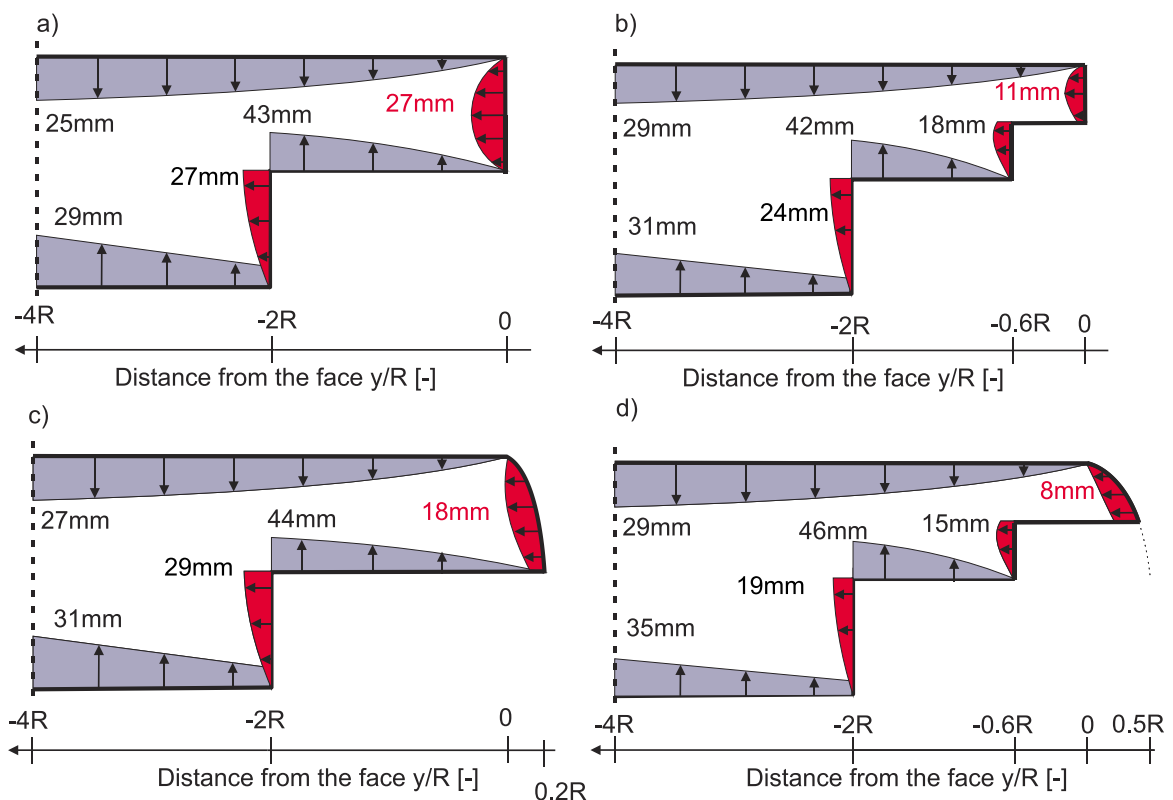


Figure 3.18: State of deformation at the face. Supported sequential excavation: a) Model A; b) Model B; c) Model C; d) Model D

Turning our attention to the state of the ground, one could observe similar trends already presented for an unsupported case. On one hand, the application of the supporting core is a tool to decrease the plastic radius. On the other hand, a comparable extent of failure zones was obtained with the spherical face (model C). Note that the model D (see

Figure 3.19d) developed the plastic zone of only 0.2R. A considerably larger plastification took place with the top heading excavation (see Figure 3.19a).

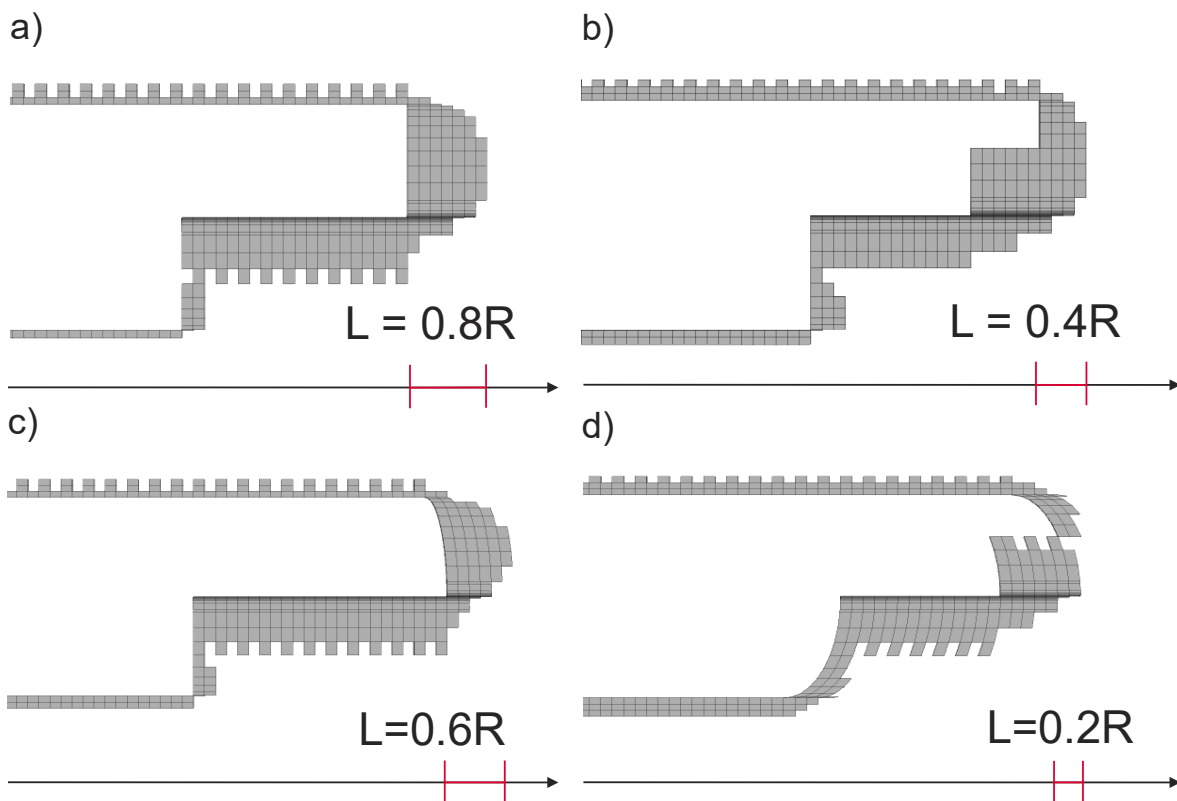


Figure 3.19: Plastic state at the tunnel face. Supported sequential excavation: a) Model A; b) Model B; c) Model C; d) Model D

3.4 Shotcrete lining with face bolting

The set of material parameter concerning face bolts can be found in Table 2.5 in subsection 2.2.3. The author chose twelve fully grouted, 12 m long bolts. Initially, simulations have been performed with the parameter set no. 1. However, due to relatively good ground conditions the results did not differ significantly from the findings presented in the subsection 3.3. Therefore, a clear statement concerning the behaviour of the spherical face could not be given. As a consequence, simulations were repeated. However, this time the parameter set no. 2 was used. Therefore, the figures below contain the results with parameter set no. 2. Still, the results obtained with the parameter set no. 1 can be found in Appendix C and Appendix D, respectively.

Firstly, Figure 3.20 illustrates the displacement plots. As expected, the calculation with the model 4 yielded the lowest amount of face extrusion. The maximum horizontal displacement reached a value of 25 mm (see Figure 3.20d). As before, a gradual decrease

of r_s caused the face displacements to increase. Hence, the simulation with the vertical face (model 1) produced the highest longitudinal displacements (see Figure 3.20a). The maximum value equalled to 96 mm.

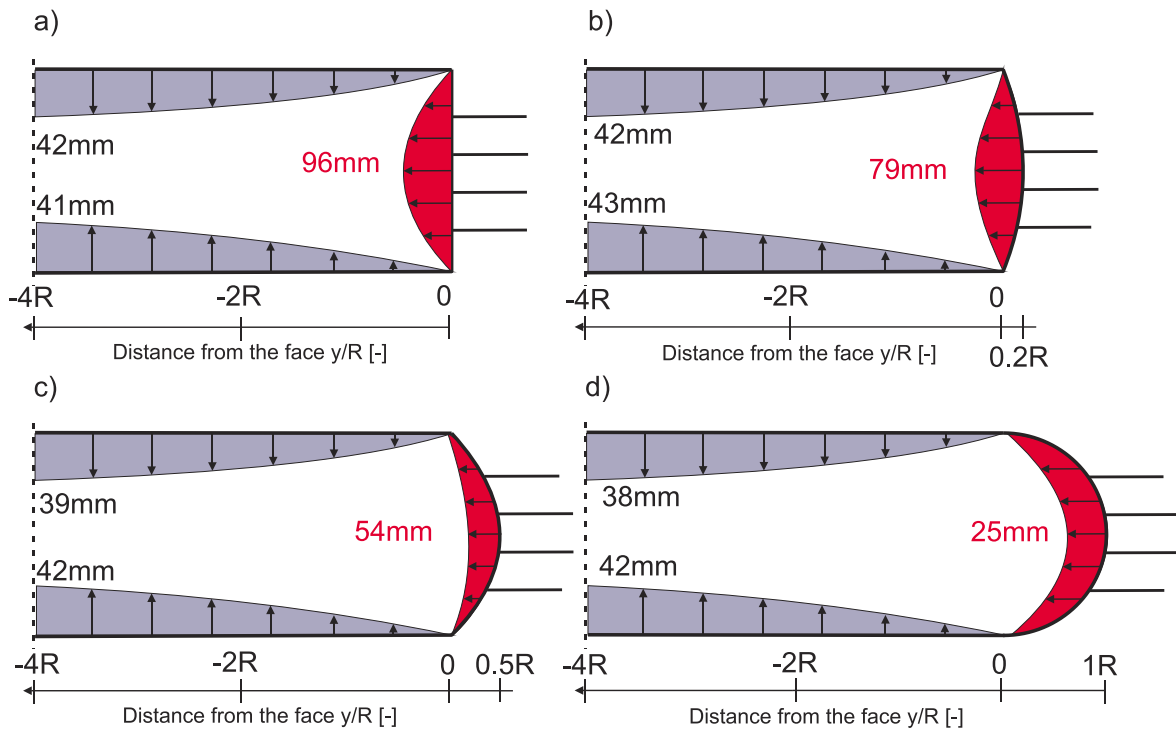


Figure 3.20: State of deformation at the face. Full face excavations supported with shotcrete and bolts: a) Model 1; b) Model 2; c) Model 3; d) Model 4

Turning our attention to failure zones, Figure 3.21 shows the extent of plastic radius for each model. Remember that the simulations were conducted with the parameter set no. 2. As such, model 4 yielded the lowest volume of the failure zone ahead of the face. While model 1 experiences a plastic zone of $2.1R$, the plastic radius of the spherical face is only $1R$ (see Figure 3.21d). Finally, the parameter r_s had only marginal influence on the plastic radius in the crown. Similarly, in the horizontal plane (x - y plane) the extent of failure zone is almost constant, regardless of the r_s value (see Figure 3.22).

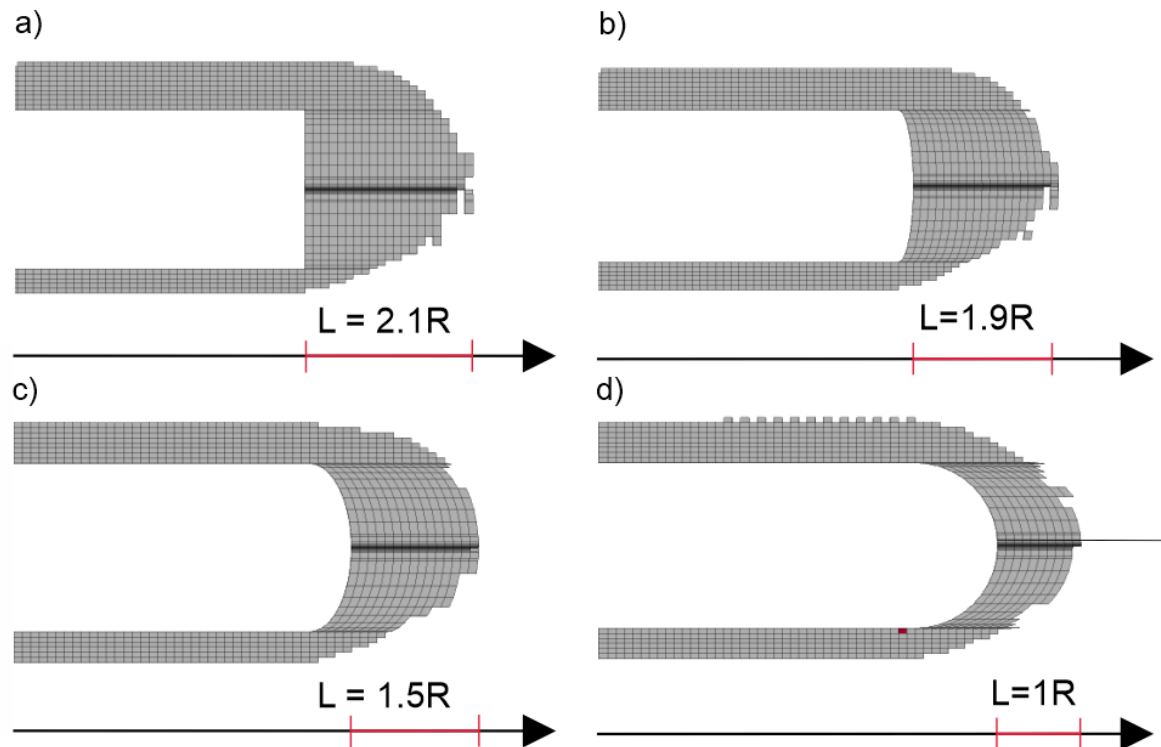


Figure 3.21: Plastic state at the face with shotcrete and face bolts. Full face excavations:
a) Model 1; b) Model 2; c) Model 3; d) Model 4

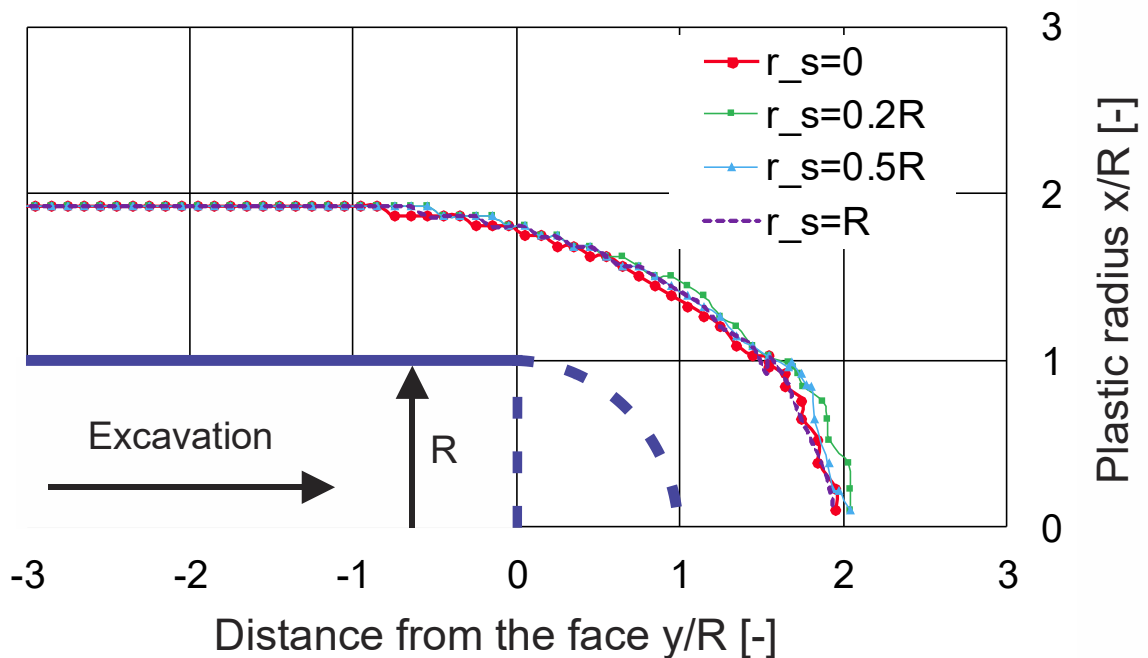


Figure 3.22: Comparison of plastic radius at the face supported with shotcrete and bolts.
Full face excavations

4 Discussion

This study revealed that the shape of the face influences the deformations of the tunnel. One of the trends that emerged from this work is that an increase of the parameter r_s leads to a decrease of the horizontal face displacements. In other words, the more rounded the tunnel face is, the lower are the deformations. This was based on cases with and without a tunnel support. In an attempt to quantitatively describe the impact of a spherical face, an additional parameter d_{red} was developed. As illustrated in Eq. (4.1), the term d_{red} expressed the ratio of face longitudinal displacements with spherical and vertical faces. The values in the nominator are the deformations at the face obtained with models 1, 2, 3 and 4. The reference value in the denominator is a displacement of an unsupported full face excavation with a vertical face (see upper right corner in Figure 4.1). The d_{red} was obtained for calculation groups I, II and III.

$$d_{red} = \frac{\text{Model 1} | \text{Model 2} | \text{Model 3} | \text{Model 4}}{\text{unsupported Model 1}} \quad (4.1)$$

To give a brief explanation, assume face displacements equal to 20 mm and 30 mm with spherical and vertical faces, respectively. Thus, the reduction factor can be obtained as follows:

$$d_{red} = \frac{20mm}{30mm} = 0.66 \quad (4.2)$$

A lower value of d_{red} means a higher displacement reduction. Hence, d_{red} can be referred as an indicator of the effectiveness.

Having defined the reduction factor, the next subsection deals with the interpretation of the findings from chapter 3. Firstly, Figure 4.1 shows the relationship between the d_{red} (vertical axis) and r_s (horizontal axis) obtained with the parameter set no. 1. Numbers in the boxes present the exact values of the d_{red} for each case. When no support is applied the spherical face ($r_s = R$) causes a reduction of the horizontal displacements by 45%. Note that the trend line for $r_s > 0.5$ approaches a constant value. This suggests that a further decrease of displacement may not take place. However, when the tunnel support is applied the reduction of displacements by 64% occurs already with the $r_s=0.5R$. Interestingly, as the r_s increases, one can observe a larger difference between the group I and II. It suggests that the face support enhances the effectiveness of the spherical face. When the r_s equals to R, the d_{red} is only 0.2. In other words, the horizontal deformation with the supported

spherical face equals to 20% of an equivalent displacement with an unsupported vertical face.

Finally, the green circular points illustrate the reduction factor obtained for the group III. As explained previously, it represents an excavation supported with a shotcrete and face bolts. Comparing to the cases with shotcrete only, face bolting helps to further reduce the displacements. Hence, the d_{red} for group III is lower than for group II. However, as the r_s increases, the difference between the green (group III) and the red line (group II) reduces. There are at least two explanations related to these results. In general, the effect of face bolting can be understood as a support pressure applied on the face. One on hand, the support pressure is a function of shear stresses at the interface between the ground and the grout (Anagnostou & Serafeimidis, 2007). On the other hand, shear stresses are influenced by the relative displacement between the bolt and the ground. As this work already shown, the spherical face experiences significantly lower face deformations than the vertical one. Lower deformations lead to a decrease of shear stresses along the tensioned element. This means that a higher parameter r_s , leads to a lower support pressure developed by bolts. The second explanation may involve the ground characteristics. Due to the assumption of relatively good ground conditions, the calculations with groups II and III yielded similar results. The values of the d_{red} obtained with the parameter set no. 2 can be found in Appendix E.

Turning our attention to a sequential excavation, Eq. (4.3) shows the formula for d_{red} . Values in the numerator refer to a horizontal displacement at the face obtained for models B, C or D, whereas the denominator is a reference displacement obtained with an unsupported top heading excavation (see upper right corner in Figure 4.2).

$$d_{red} = \frac{\text{Model B} \mid \text{Model C} \mid \text{Model D}}{\text{unsupported Model A}} \quad (4.3)$$

The bar chart in Figure 4.2 illustrates the reduction factor d_{red} of a sequential excavation. It is shown that the application of a supporting core reduces the displacements at the face by 24%. However, when the lining is applied, the reduction factor equals only 0.33. Interestingly, the reduction factors of the supported model A and unsupported model C are equal. Similarly, model D without support yielded only slightly higher displacements than the model B with face support. Finally, note that model D yields the lowest d_{red} . The values of d_{red} for unlined and lined tunnels equal to 0.39 and 0.24, respectively.

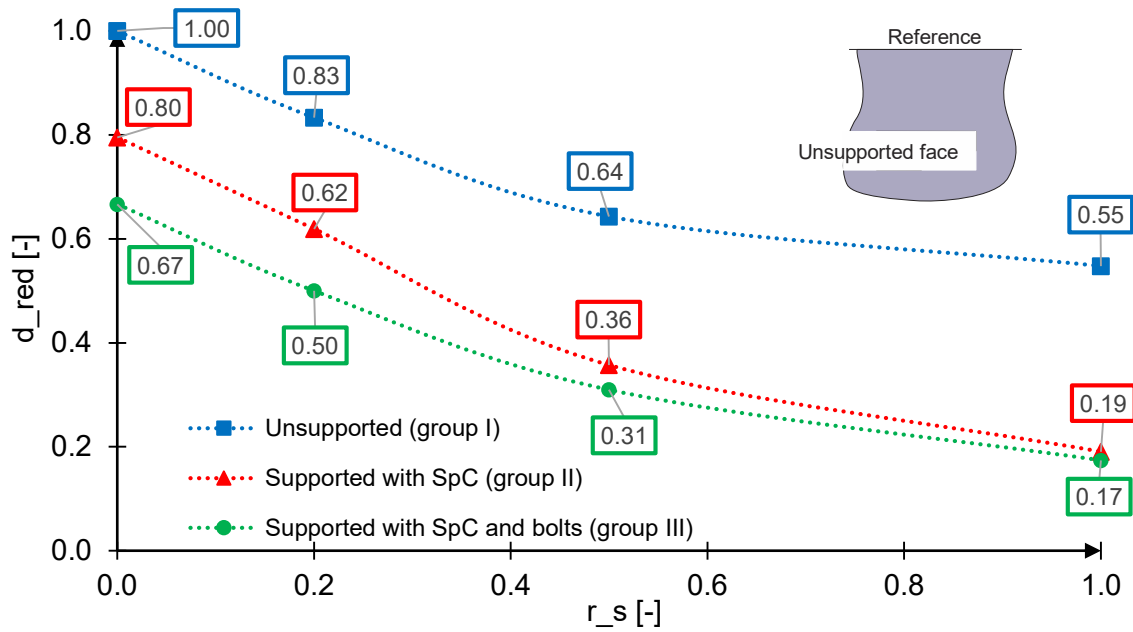


Figure 4.1: The reduction factor d_{red} as a function of the r_s . Full face excavations

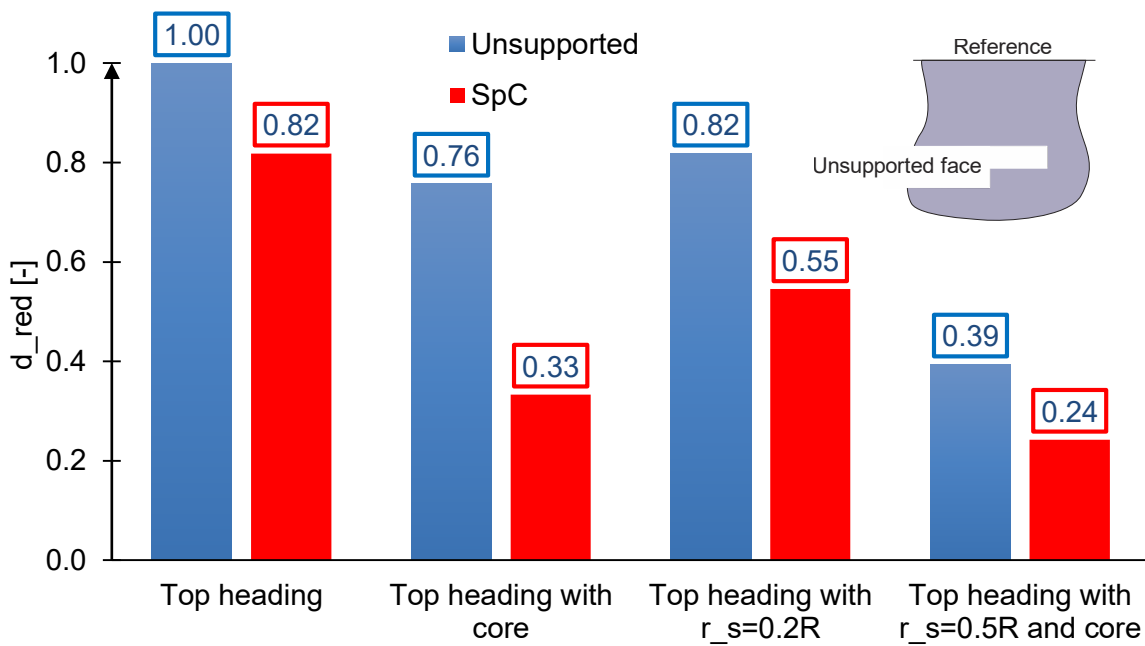


Figure 4.2: The reduction factor d_{red} depending on the type of the sequential excavation

A careful reader noticed that the spherical face supported with shotcrete yielded lower d_{red} than the vertical face supported with lining and bolts. This led to a question, if a similar trend can be achieved in poor ground conditions. An additional series of calculations was performed in an attempt to answer this question. A soft ground was simulated using the parameter set no. 2 (see Table 2.2 and Table 2.3, Section 2.2.1). The calculations were performed with the Mohr-Coulomb and the Plastic Hardening constitutive models.

Poor ground conditions caused a collapse of an unsupported tunnel. Hence, the next simulation (model A) dealt with a full face excavation supported with shotcrete (see Figure 4.3a). However, as Figure 4.4 illustrates, the longitudinal deformation at the face exceeded 22 cm. Furthermore, 10 cm of a vertical deformation ahead of the face was observed. Therefore, a failure was assumed. Hence, in the third calculation twelve face bolts were simulated (see Figure 4.3b). The parameters concerning bolts can be found in Table 2.5 in section 2.2.3. In the next step, to validate the hypothesis presented in the previous paragraph, a simulation of the full face excavation with a spherical face has been performed. While the face was supported only with shotcrete, the parameter r_s was equal to $0.5R$ (see Figure 4.3c). Finally, to illustrate the positive impact of a sequential excavation, the fourth simulation considered a top heading with a spherical face and a supporting core (see Figure 4.3d). The parameter r_s was equal to $0.5R$, same as the core length.

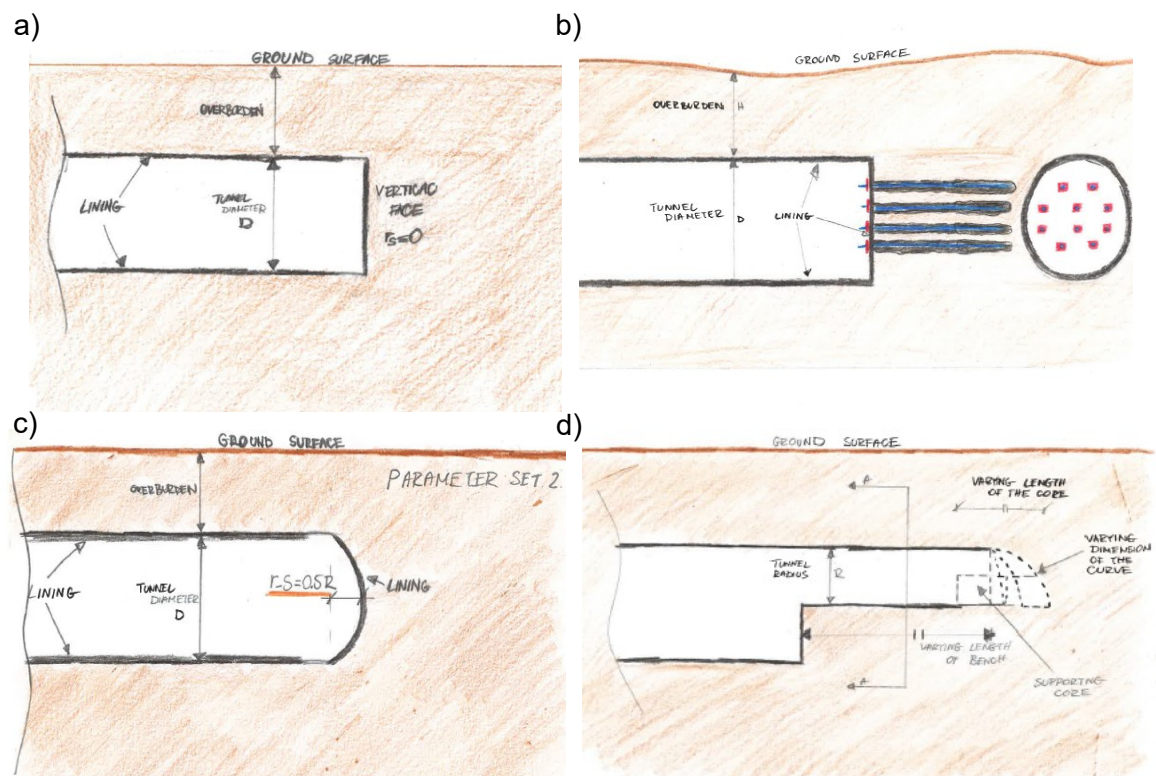


Figure 4.3: a) Full face excavation supported with shotcrete (model A); b) Full face excavation supported with shotcrete and face bolts (model B); c) Spherical full face excavation supported with shotcrete (model C); d) Top heading excavation supported with shotcrete and supporting core (model D)

Figure 4.5a reveals the state of deformation at the face with the model B. Compared to the model A, longitudinal displacement at the face was reduced by 126 mm. In addition, vertical deformation at the crown and in the invert decreased by 65 mm and 29 mm, respectively. Interestingly, as shown in Figure 4.5b, closely matched deformations occurred

with the model C. To be specific, the spherical face yielded 10 cm longitudinal displacement at the face. Moreover, comparing to the model A, the displacements at the crown and in the invert have been reduced by 47 mm and 18 mm, respectively. Thus, a confirmation of the findings presented in Figure 4.1 was provided.

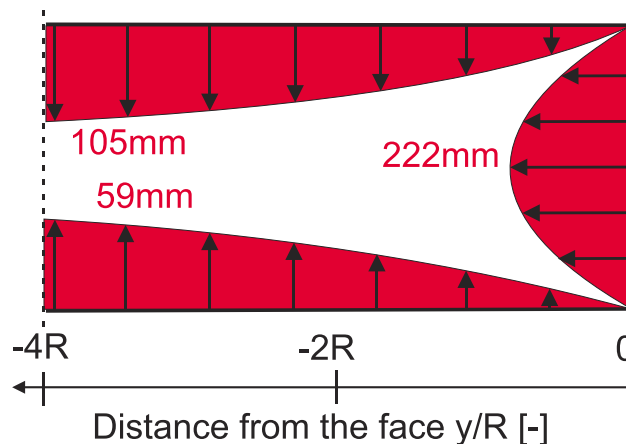


Figure 4.4: Deformation at the face with the Mohr-Coulomb. Model A

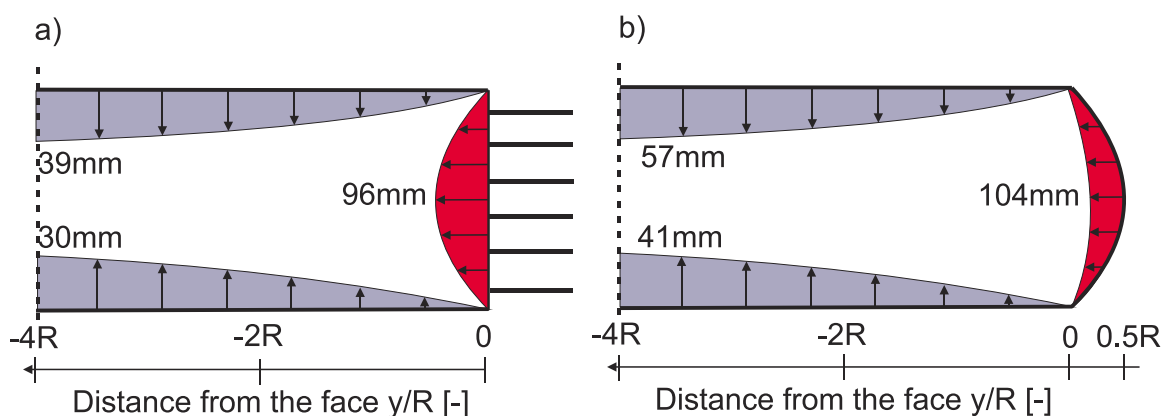


Figure 4.5: Deformation at the face with the Mohr-Coulomb: a) Model B; b) Model C

As Figure 4.6 illustrates, the lowest face deformations were obtained with the model D. As compared to the model A, the horizontal displacements at face have been reduced by 177 mm. Large deformation of the bench have been reduced with the application of support. However, due to large deformations in the sidewall, two rows of bolts with $L_a = 6\text{ m}$ were required.

Calculations with the Plastic Hardening soil model shows a similar trend. Still, the deformations were notably lower comparing to the simulations with Mohr-Coulomb. Maximum horizontal deformation with the model A only slightly exceed 12 cm (see Figure 4.7). Models B and C yielded a longitudinal face displacement of 52 mm and 43 mm,

respectively (see Figure 4.8). One of the reasons for that may be the increase of the ground stiffness E_{ur}^{ref} . According to Itasca (2017), the unloading/reloading stiffness E_{ur}^{ref} has to be at least two times higher than the secant modulus E_{50}^{ref} . Nevertheless, the findings confirmed previously stated hypothesis. In the given ground conditions the spherical face could achieve comparable face displacements as the planar face additionally supported with face bolts.

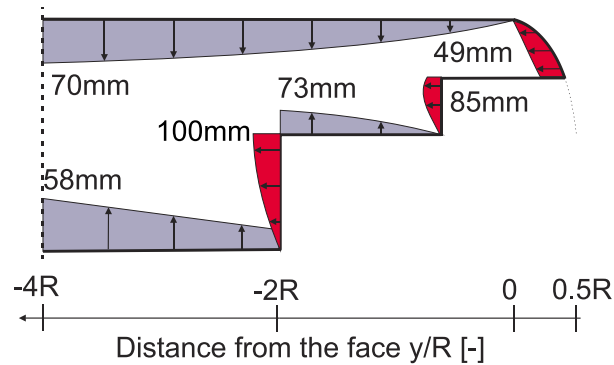


Figure 4.6: Deformation at the face with the Mohr-Coulomb. Model D

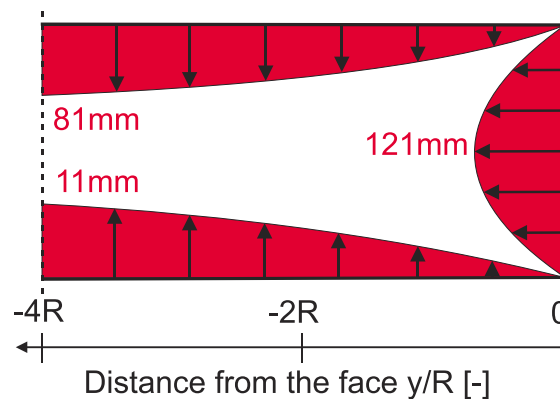


Figure 4.7: Deformation at the face with the Plastic Hardening. Model A

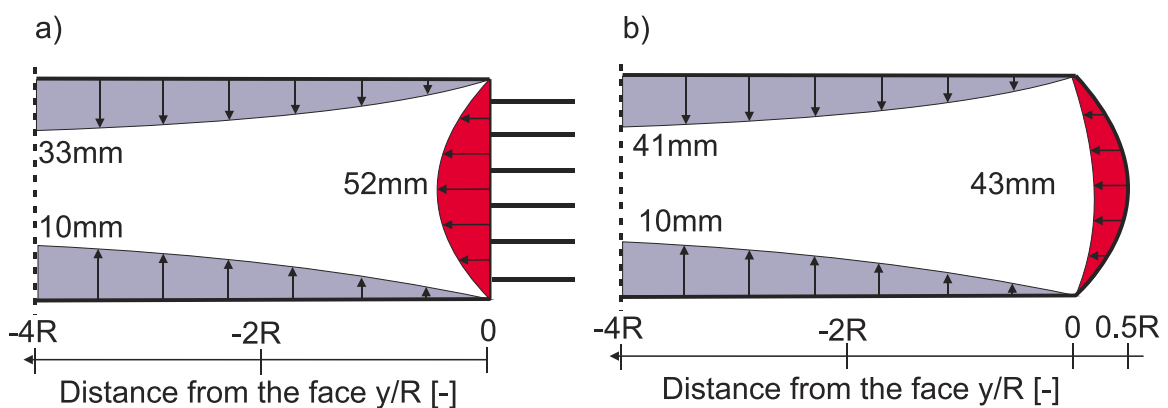


Figure 4.8: Deformation at the face with the Plastic Hardening: a) Model B; b) Model C

5 Conclusion

5.1 Summary

This thesis was elaborated to compare the behaviour of planar and spherical faces in the context of conventional tunnelling. To date there has been only few studies dealing comprehensively with this topic. Therefore, the author made an attempt to combine the analysis of secondary stresses and deformations. A particular emphasis was placed on the development of the load-bearing arch ahead of the face. Collapse mechanisms as well as the dimensions of failure zones have been compared. To achieve the objectives a series of three-dimensional simulations using a FDM software was performed. The developed models covered the range of staged and full face excavations.

The background of this work was provided in the introduction. Selected calculation procedures, including failure mechanisms, have been presented. Finally, the author summarized a number of studies which dealt with a spherical face to date.

Chapter 2 gave an insight into the methodology used in this thesis. As a part of this section the model geometry, material parameters, boundary conditions and applied constitutive models have been shown. In addition, the scope of the numerical analysis was illustrated. Finally, the model validation confirmed that the developed programme yields plausible results.

Chapter 3 dealt with the results of the numerical simulations. Firstly, this work demonstrated that the application of the spherical face leads to a reduction of displacements at the face. Secondly, the findings of this thesis suggested that the load-bearing arch develops closer to the excavation contour than with a planar face. Thirdly, the simulations with a tunnel support showed a decrease of lining forces with the spherical face. While the stress state ahead of the heading was almost identical, face deformations were significantly reduced. Finally, the volumes of plastic zones decreased.

Furthermore, it has been observed that the spherical face yields lower face deformations than a top heading excavation with an auxiliary bench. Hence, the findings of Kusumoto et al. (2013) have been confirmed. Still, the positive impact of a staged excavation on the tunnel deformations has been revealed. A careful reader noticed a reduction of displacements ahead of the face. It was also shown that the supporting core

enhances the stability of the face. Interestingly, with the spherical face a comparable state of deformation can be achieved as with the vertical face supported with a core.

Finally, using a dimensionless parameter d_{red} it was possible to quantify the effectiveness of the spherical face. In a soft ground the spherical face yielded similar deformations as the vertical face supported with bolts. Hence, the necessity of bolts could be eliminated. Even lower displacements occurred with the top heading excavation with a spherical face. This method caused the reduction of face deformations by a factor of five. Therefore, this excavation type is suitable for tunnelling in poor ground conditions. The lack of face bolts accelerates the excavation process and reduces the material demands.

5.2 Outlook

Nevertheless, due to the number of important limitations this work does not exclude further studies concerning a spherical tunnel face. Firstly, the conclusions stated in this work are valid only for a homogeneous, isotropic ground. Secondly, a circular tunnel cross section was assumed. Thirdly, a time-dependent behaviour of the tunnel support has not been modelled. As such, the lining exhibited an elastic behaviour. This assumption, however, does not comply with the reality. Finally, the majority of simulations have been conducted with the Mohr-Coulomb constitutive model. As already mentioned, the constant soil stiffness poses a significant drawback of this method. To summarize, further research may explore the following topics:

- Evaluation of the spherical face behaviour based on an example of a deep tunnel with high in-situ stress level
- Application of a high order constitutive model of tunnel lining. This could include a simulation of a time-dependant behaviour (i.e. creep, strength and stiffness increase)
- Onsite feasibility study to determine an optimal value of the parameter r_s
- Analysis of the cost-related subjects such as: material demand, number of workforces, excavation machines
- Analysis of the operational-related topics such as: excavation procedure in poor ground conditions, time requirements and necessary modification of excavation machines

- Behaviour of the spherical face with the other types of tunnel support such as: pipe umbrella system, bolts, ground freezing or jet grouting
- Investigation into the influence of geotechnical parameters on the reduction factor d_{red}

Bibliography

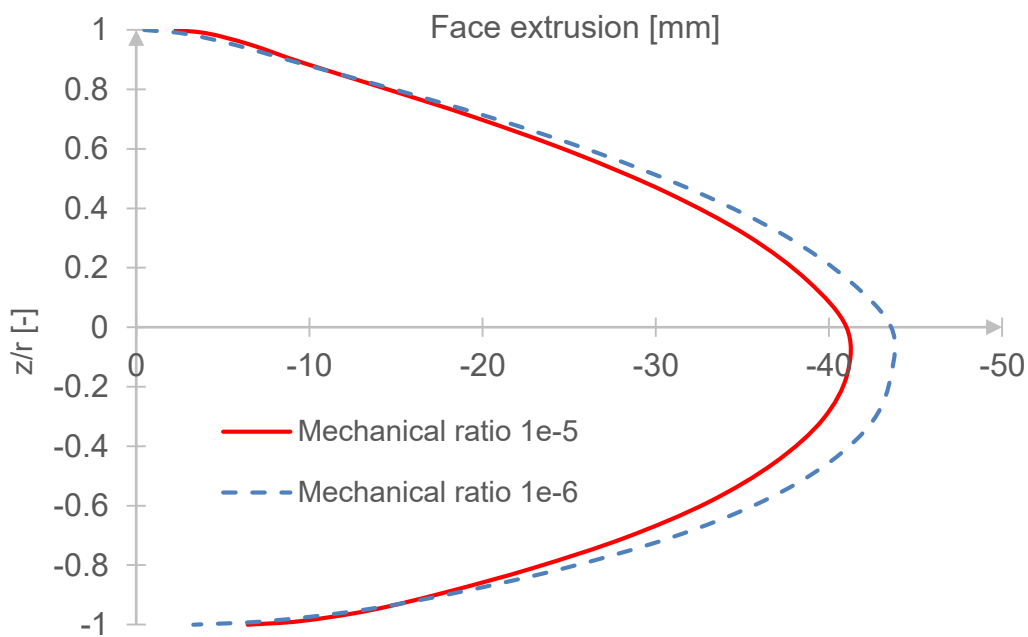
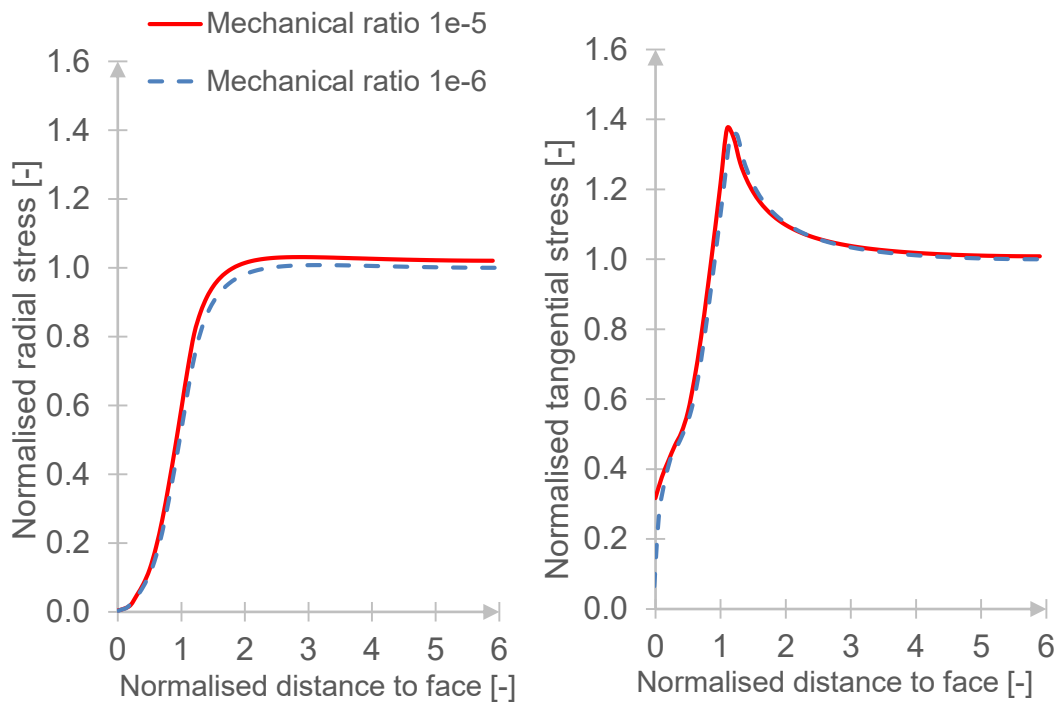
- Amemiya, K., Kakimi, K., Kusumoto, K. & Sasaki, T.** 2014. Application of a spherical tunnel face to full-face tunnel excavation by drill and blast. In: *Proceedings of the 8th Asian Rock Mechanics Symposium. Rock Mechanics for Global Issues – Natural Disasters, Environment and Energy*, Sapporo, Japan, 14.-16. October 2014.
- Ahrens, H., Lindner, E. & Lux, K.-H.** 1982. Zur Dimensionierung von Tunnelausbauten nach den Empfehlungen zur Berechnung von Tunneln im Lockergestein. *Bautechnik* 59, Heft 8, S.260-273
- Anagnostou, G. & Serafeimidis, K.** 2007. The dimensioning of tunnel face reinforcement. In: *Proceedings of ITA World Tunnel Congress 2007. Underground Space – The 4th dimension of metropolises*, Prague, Czech Republic, 5.-10. May 2007, Taylor & Francis Group: London.
- Atkinson, J. H. & Potts, D. M.** 1977. Stability of a shallow circular tunnel in cohesionless soil. *Géotechnique* 27 (2), S. 203-215
- Atkinson, J. H. & Mair, R. J.** 1981. Soil mechanics aspects of soft ground tunneling. *Ground Engineering* 14 (5), S. 20-38
- Broere, W.** 2001. Tunnel face stability & New CPT applications. PhD thesis, Chair of Underground Space Technology, Delft University of Technology, Netherlands.
- Cantieni, L.** 2011. Spatial Effects in Tunnelling Through Squeezing Ground. PhD thesis, Institut für Geotechnik, ETH Zürich, Zürich, Switzerland
- Carranza-Torres, C. & Fairhurst, C.** 2000. Application of Convergence-Confinement method of tunnel design to rock masses that satisfy the Hoek-Brown failure criterion. *Tunneling and Underground Space Technology* 12 (2), S. 187-213
- Do, N. A., Dias, D., Oreste, P. & Djeran-Maigre, I.** 2013. Comparison between Design Methods Applied to Segmental Tunnel Linings. *Geotechnical Engineering Journal of the SEAGS & AGSSEA*. Vol. 44, December 2013.
- Deutsche Gesellschaft für Geotechnik** 2012. *Empfehlung des Arbeitskreises "Numerik in der Geotechnik" EANG*. Verlag Ernst & Sohn: Berlin.
- Einstein, H. H. & Schwartz, C. W.** 1979. Simplified Analysis for Tunnel Supports. *Journal of the Geotechnical Engineering Division* 105, S. 499-517.
- Feder, G. & Arwanitakis, M.** 1976. Zur Gebirgsmechanik ausbruchsnaher Bereiche tiefliegender Hohlraumbauten (unter zentralsymmetrischer Belastung. *Berg- und Hüttenmännische Monatshefte*, Jahrgang 121, Heft 4.

- Golser, H.** 2001. Die Anwendung der Method der finiten Element und Randelemente im Tunnelbau. Dissertation, Institut für Felsmechanik und Tunnelbau, Technische Universität Graz, Österreich.
- Horn, N.** 1961. Horizontaler Erdruck auf senkrechte Abschlussflächen von Tunnelröhren. In: *Landeskonferenz der ungarischen Tiefbauindustrie*, Budapest, Hungary.
- Itasca** 2017. *FLAC^{3D} 6.0 Fast Lagrangian Analysis of Continua in 3 Dimensions*. User's manual. Itasca Inc., Minneapolis, USA.
- Jaky, J.** 1944. The coefficient of earth pressure at rest. *Journal for Society of Hungarian Architects and Engineers*, S. 355-358
- Kirsch, A.** 2015. Numerical investigation of the face stability of shallow tunnels in sand. In: *Proceedings of the 7th European Conference on Numerical Methods in Geotechnical Engineering NUMGE 2010 – Numerical Methods in Geotechnical Engineering*, Benz, T. & Nordal, S. (eds.), Trondheim, Norway, 2.-4. June 2010, S. 779-784. Taylor & Francis Group: London.
- Kolymbas, D.** 1998. *Geotechnik – Tunnelbau und Tunnelmechanik. Eine systematische Einführung mit besonderer Berücksichtigung mechanischer Probleme*. Springer-Verlag: Berlin, Heidelberg.
- Krause, T.** 1987. Schildvortrieb mit flüssigkeits- und erdgestützter Ortsbrust. In: *Report of the Institute of Geotechnical Engineering of the University of Braunschweig*, No. 24.
- Kusumoto, F., Tanimura, K. & Sato, J.** 2013. The effect of hemi-spherical tunnel face on the stability of mountain tunnels. In: *Proceedings of the World Tunnel Congress - Underground. The Way to the Future*, Anagnostou, G. & Ehrbar, H. (eds.), Geneva, Switzerland, May 31-June 7, 2013, S. 685-692. Taylor & Francis Group: London.
- Leca, E. & Dormieux, L.** 1990. Upper and lower bound solutions for the face stability of shallow circular tunnels in frictional material. *Géotechnique* 40 (4), S. 581-606.
- Meißner, H.** 1991. Empfehlungen des Arbeitskreises „Numerik in der Geotechnik“ der Deutschen Gesellschaft für Erd- und Grundbau e.V. *Geotechnik* 14, S. 1-10.
- Meißner, H.** 1996. Tunnelbau unter Tage. Empfehlungen des Arbeitskreises 1.6 “Numerik in der Geotechnik”, Abschnitt 2, *Geotechnik* 19 (2),
- Papakonstantinou, S.** 2008. Technical and economical comparison between full face and sequential excavation. Dissertation, Institut für Felsmechanik und Tunnelbau, Technische Universität Graz, Österreich.
- Rocscience: RS2** 2017. User manual. Rocscience Inc., Ontario, USA

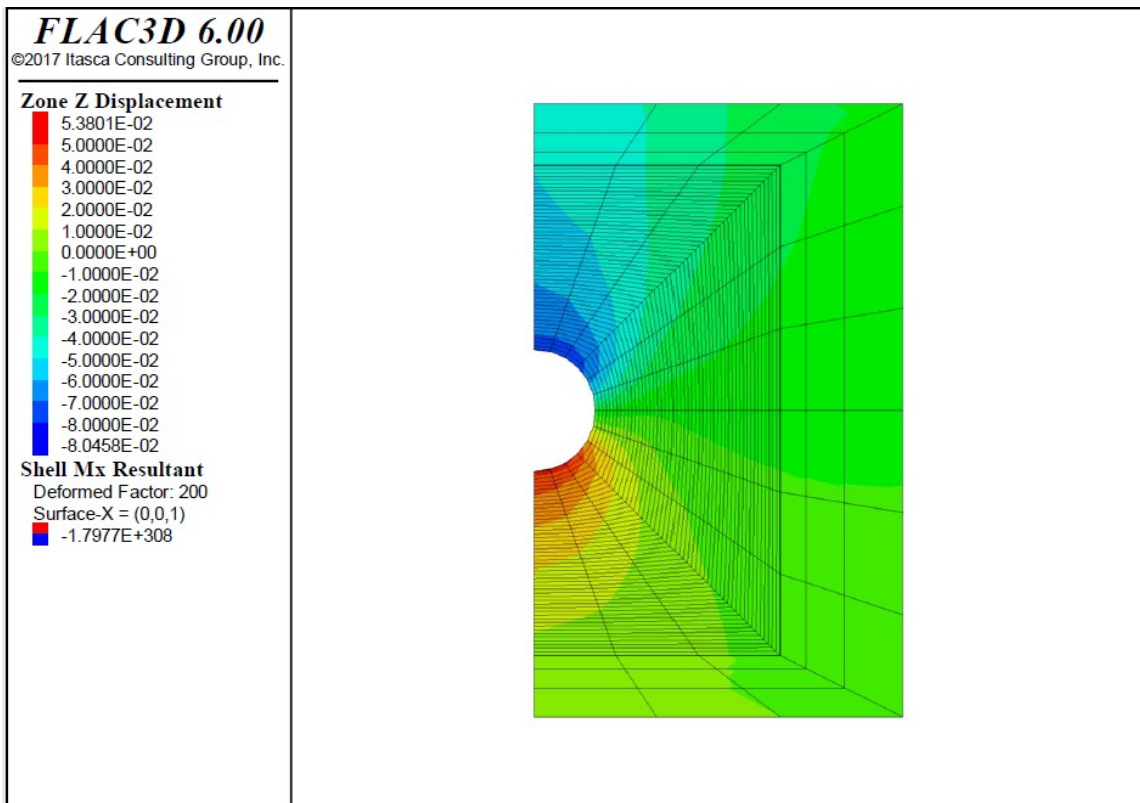
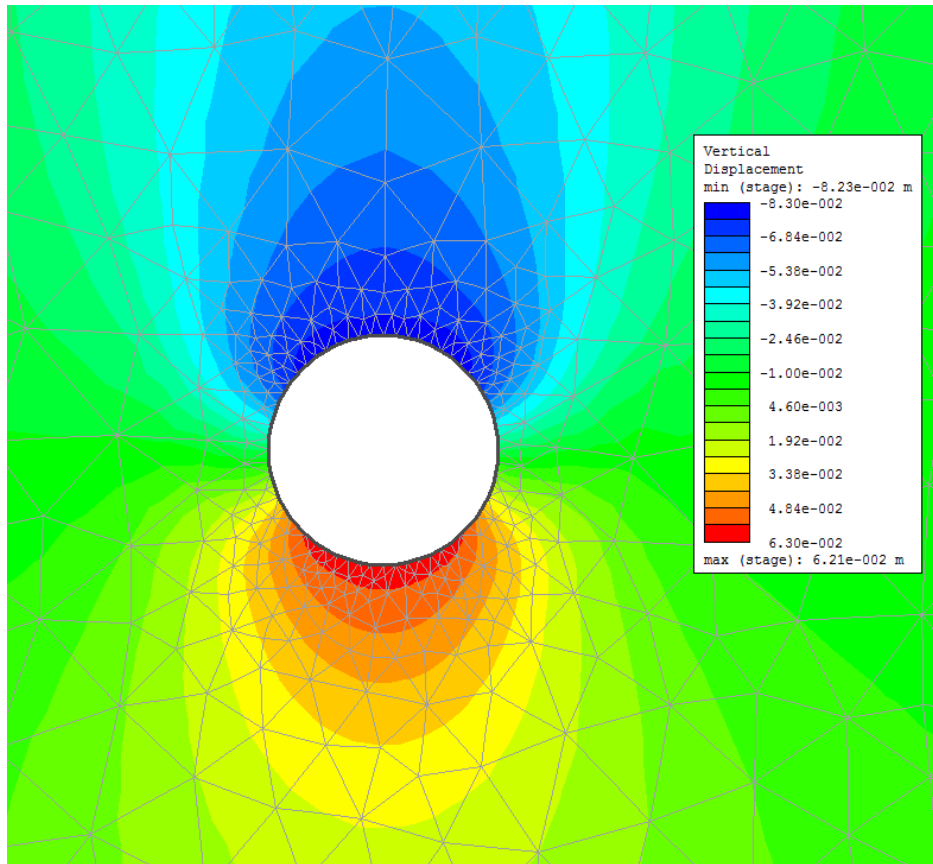
- Ruse, N. M.** 2004. Räumliche Betrachtung der Standsicherheit der Ortsbrust beim Tunnelvortrieb. Dissertation, Institut für Geotechnik, Universität Stuttgart, Deutschland.
- Schubert, P. A. & Schweiger, H. F.** 2004. Zur Standsicherheit der Ortsbrust in Lockerböden. In: *Proceedings of the ISRM regional symposium Eurock 2004 & 53rd Geomechanics Colloquy - Rock Engineering. Theory and practice*, Schubert, W. (ed.), Salzburg, Austria, 6.-8. October 2004, S. 99-104. Verlag Glückauf: Essen.
- Shinji, M., Morimoro, S. & Nakagawa K.** 2004. Evaluation on the stability of tunnel face in weak rock based on the three-dimensional numerical analysis. In: *Proceedings of the ISRM regional symposium Eurock 2004 & 53rd Geomechanics Colloquy - Rock Engineering. Theory and practice*, Schubert, W. (ed.), Salzburg, Austria, 6.-8. October 2004, S. 151-154. Verlag Glückauf: Essen.
- Sternath, R. & Baumann, Th.** 1997. Face support for tunnels in loose ground. In: *Tunnels for people: Proceedings of World Tunnel Congress '97 and 23rd General Assembly of the International Tunnelling Associations*, Golser, J., Hinkel, W. & Schubert, W. (eds.), Vienna, Austria, 12.-17. April 1997, S. 317-324. AA Balkema: Rotterdam.
- Wittke, W.** 1999. *Tunnelstatik Grundlagen: Geotechnik in Forschung und Praxis, WBI-Print 4*. S. 62-137. Verlag Glückauf: Essen.
- Wittke, W.** 1984. *Felsmechanik – Grundlagen für wirtschaftliches Bauen im Fels*. Springer Verlag: Berlin, Heidelberg, New York, Tokyo.
- Vermeer, P. A., Ruse, N. M. & Marcher, T.** 2002. Tunnel Heading Stability in Drained Ground. *Felsbau* 20 (6), S. 8-18.

Appendix

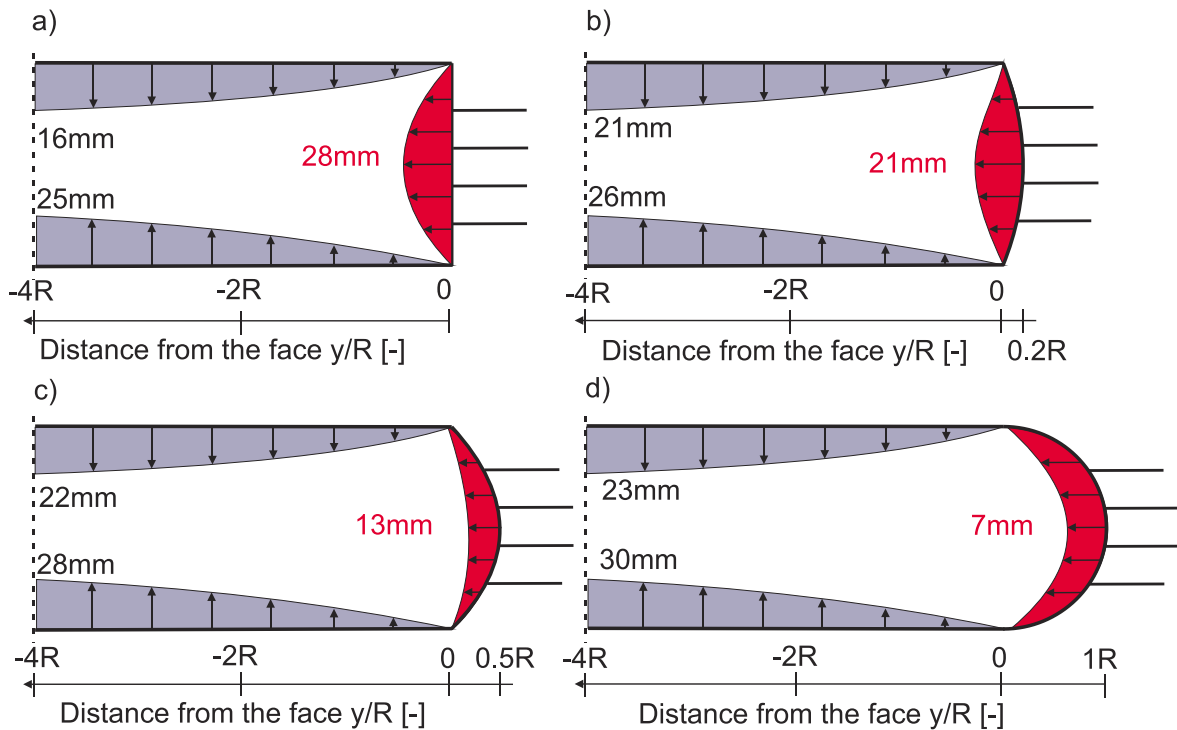
Appendix A: Influence of mechanical ratio on stress and deformational state



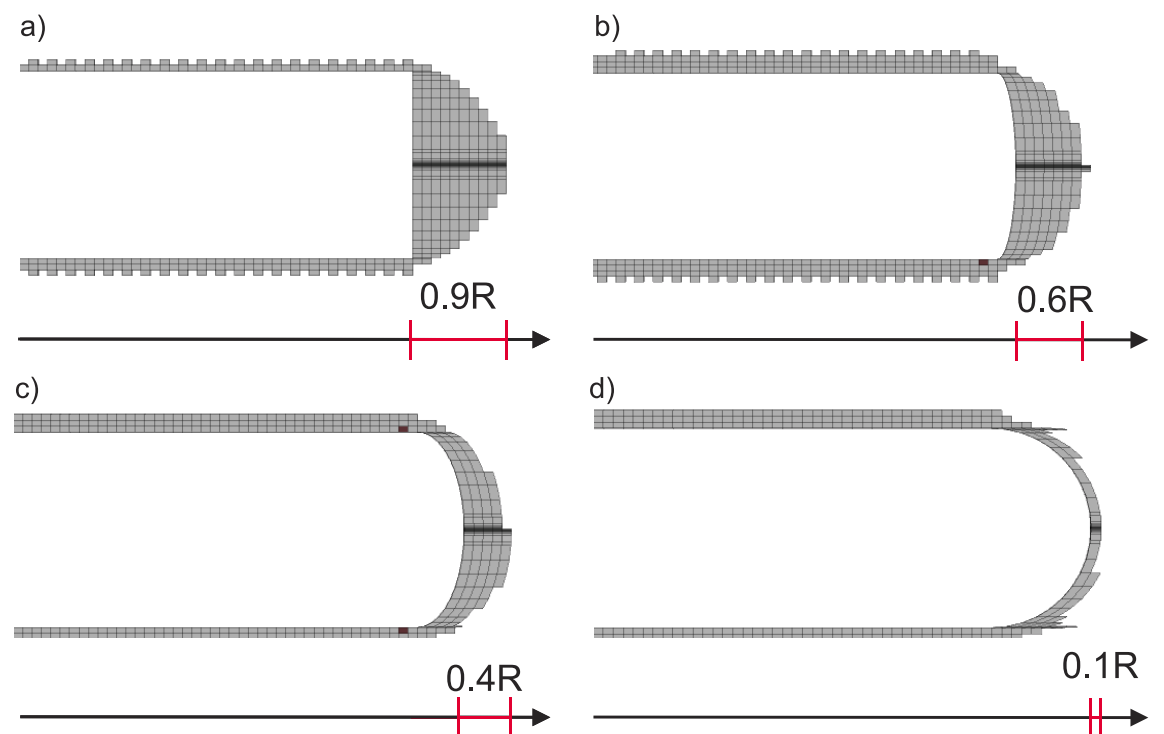
Appendix B: 2D calculation with FE software (RS²) and plain strain model with FLAC 3D



Appendix C: State of deformation at the face. Full face excavation supported with shotcrete and bolts. Material parameter set no. 1: a) Model 1; b) Model 2; c) Model 3; d) Model 4



Appendix D: Plasticity state at the face. Full face excavation supported with shotcrete and bolts. Material parameter set no. 1: a) Model 1; b) Model 2; c) Model 3; d) Model 4



Appendix E: Reduction factor d_{red} as a function of the parameter r_s valid for group III with material parameter set no. 2

